CO_2 Degassing and Metal Enrichments During Magma-Carbonate Interactions in the Jurassic Bonanza Arc

by

Graham Arndt

A Thesis Submitted in Partial Fulfillment of the
Requirements of the

HONOURS PROGRAM

in the School of Earth and Ocean Sciences

Supervisors: Dante Canil and Rebecca Morris

University of Victoria

We acknowledge and respect the Lək̓ʷəŋən (Songhees and Xʷsepsəm/Esquimalt) Peoples on whose territory the university stands, and the Lək̓ʷəŋən and W̱SÁNEĆ Peoples whose historical relationships with the land continue to this day.

1. Acknowledgements

I would like to first acknowledge my supervisor, Dr. Dante Canil. Dr. Canil was an insightful mentor and provided me with valuable guidance, constructive criticism, and motivation to complete my thesis. Furthermore, he taught me important petrological techniques during my experimental process that I can utilize in future research. I would also like to thank my co-supervisor Rebecca Morris for her outstanding inspiration and willingness to allow me to conduct research at Merry Widow along side her. Rebecca was very supportive in the lab and helped direct my research during writing. I am also grateful for Rebecca and Dante for collecting additional dyke samples in the field so I could conduct my thesis research. Finally, I would like to thank Jody Spence for his generosity, allowing me to gather my geochemistry data using his LA-ICP-MS instrument on multiple occasions. This research study was funded by the Jamie Cassels Undergraduate Research Award (JCURA).

2. Abstract

The long term (>1 Myr) atmospheric carbon budget is dominated by the carbon cycle and has great implications on habitability. One potential source of degassed carbon can be derived from the overlying continental plate where CO_2 is produced from magma-carbonate interactions. Limestone assimilation is a local process that is relegated to the vicinity of the sidewall around a magma chamber (Iacono Marziano et al., 2008). As such, the network of dykes and sills offer more surface area to interact with carbonate rock opposed to voluminous plutons. Meter-scale dyke and sill samples from the Jurassic Bonanza Arc were collected from the Merry Widow Mountain region to quantify the degree of limestone assimilation. Two types of samples were investigated: (1) bulk rock samples and (2) milli-slices sampled from a single 25 cm cross-section of dyke 79B. Major and trace element chemistry was gathered by LA-ICP-MS. We discovered that the dykes show anomalous elemental abundances for Sr, U, MnO_2, and Na_2O. In particular, the dykes appear super-enriched in Sr opposed to their parent basalt and limestone endmembers. The enriched Sr concentrations can be explained using a binary mixing model which indicates that the dykes assimilated up to 80 wt% limestone from a primitive carbonate source. This magnitude of limestone assimilation could generate up to 35 wt% CO_2 during the decarbonization of limestone into basaltic dykes.

Furthermore, limestone assimilation causes desilication and calcium enrichment of the basaltic melt adjacent to the contact region (Barnes et al., 2005; Iacono Marziano et al., 2008,). Consequently, this change in melt chemistry enhances the dyke's sulfur saturation limit and therefore its capacity to transport sulfur species. SCSS calculations indicate that the dyke contact may hold up to three times more sulfur than the dyke interior as the result of partial assimilation by limestone. An increase in sulfur saturation has important implications because it can assist in the partitioning of chalcophile elements out of a silica-rich melt, and the dissolved sulfur species can later be degassed at volcanic arcs which impacts global climate (McLinden et al. 2016; D'Souza & Canil, 2018). Overall, sulfur saturation can help model the process by which sulfide immiscibility melts form in a magma body which is a critical step in the development of ore deposits (Haldar, 2018).

Table of Contents

3. Introduction

The long term (>1 Myr) atmospheric carbon budget is dominated by the carbon cycle and has great implications on habitability. Certain periods of history such as the late Cretaceous show elevated CO_2 levels and dramatic warming, one origin of which has been suggested as a rise in arc volcanism. More recent evidence suggests that arcs are proposed sources of increased CO_2 output, but the amount, extent, and source of that CO_2 is debated (Mason et al., 2017). One source of degassed carbon is from the subducted slab, while another is from the overlying plate where CO_2 is derived from magma-wallrock interactions (Kelemen & Manning, 2015; Wong et al., 2019). Outgassed CO_2 from the overlying plate is sourced from decarbonization reactions of carbonate rock during assimilation with magma (Figure 1). The mechanisms for this process can be readily observed in the field where intrusive rocks interact with wallrock carbonates. Previous studies have focused on carbonate assimilation within km-scale plutons (Chadwick et al., 2007; Lee et al., 2013), however less study has been completed on smaller m-scale magma bodies, such as dykes and sills which is the focus of this thesis. Here, I will be using geochemical analysis to quantify the degree of limestone assimilation, and therefore CO_2 production, within basaltic dykes that transit arc crust.

In addition, limestone assimilation into melt causes an intense chemical reaction that may impact the sulfide saturation of a melt. This is done by changing the chemical composition and thus the thermodynamic properties of the melt. Sulfur species play an important role in the precipitation of chalcophile elements such as Cu, Pb, Zn (D'Souza & Canil, 2018). In some cases, precipitation of these ore metals can form a skarn deposit which can be a prospective source of base metals (Haldar, 2018). This thesis will also briefly examine how limestone assimilation impacts the saturation limit of sulfur species within dykes.

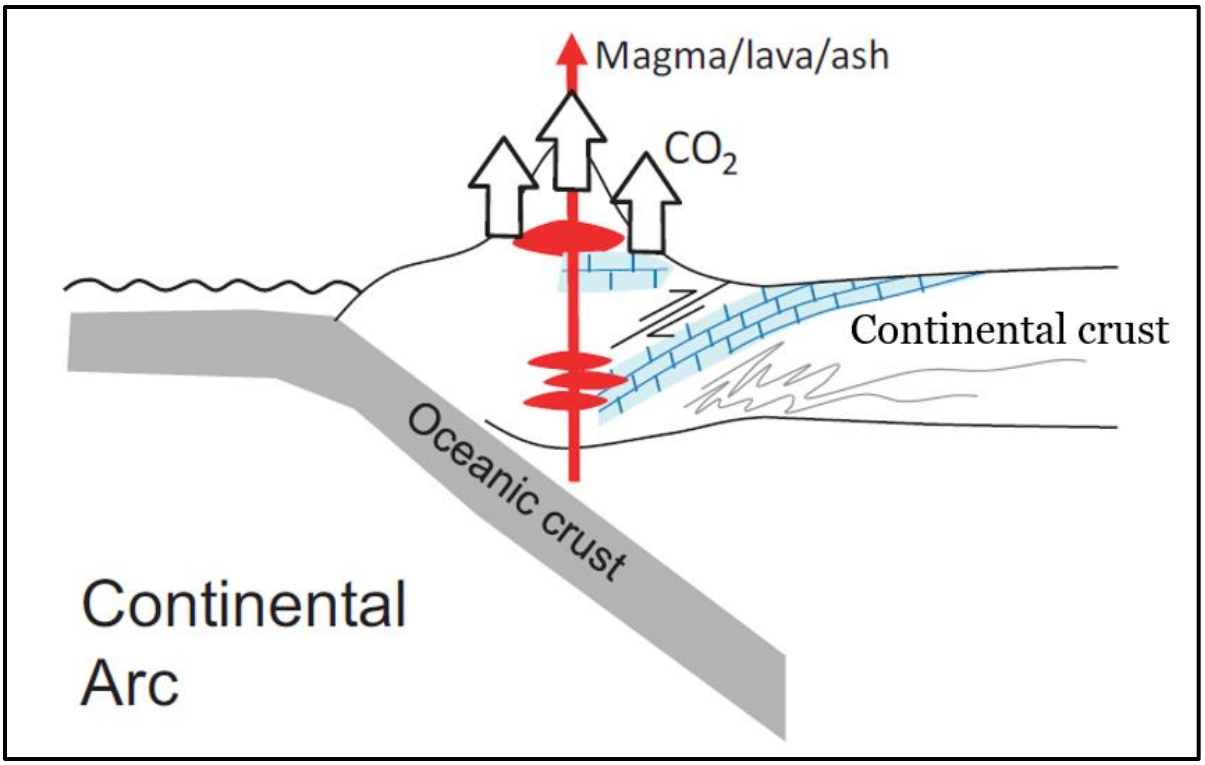

Figure 1: Generation of volcanic sourced CO_2 within the overlying continental crust at an arc setting. Arc magma intrudes ancient carbonate platform and assimilates. Decarbonation of carbonate rock produces CO_2 that is degassed. Image modified from Lee et. al. 2013.

4. Geological Background

To explore magma-carbonate interactions in the subsurface, the Jurassic Bonanza Arc on Vancouver Island, Canada is used as a local example where basaltic magma intrudes limestone of the underlying Triassic Quatsino Formation. The study area is within the Merry Widow Mountain region of northern Vancouver Island, British Columbia, Canada, located ~40km southwest of Port McNeill (Figure 2). The Merry Widow region exposes basement rocks that are a part of the Wrangellia terrane. The Wrangellia terrane stratigraphy is made up of Devonian Sicker Group volcanics, the Karmutsen flood basalts, and the late Triassic Quatsino limestone Formation (Greene et al., 2009; Jones et al., 1977). This basement was then intruded and overlain by the Jurassic Bonanza Arc that was active between 202-168 Ma (Canil et al., 2010). The region southeast of Merry Widow Mountain hosts the abandoned Empire Mine – an open pit mine which extracted Fe-Cu-Au ore from skarn localities at the contact of the Merry Widow pluton (197 Ma) and Quatsino limestone wallrock (Ray and Webster, 1991). The site provides an accessible exposure of the upper 3 km of the Bonanza Arc and preserves the details of contacts of mafic dykes and sills with wallrock carbonates (Canil and Morris, 2023). During the emplacement of the Bonanza Arc, magma intruded the Quatsino limestone platform (~1km thick) and preserved a record of magma-carbonate interactions at shallow depths (<0.2 GPa). The focus of this study is an examination of carbonate interaction and assimilation process by a study of the geochemistry of the dykes and sills at a variety of spatial scales. These dykes and sills show previously unobserved element enrichments documented at the microscale (Morris et al, 2023).

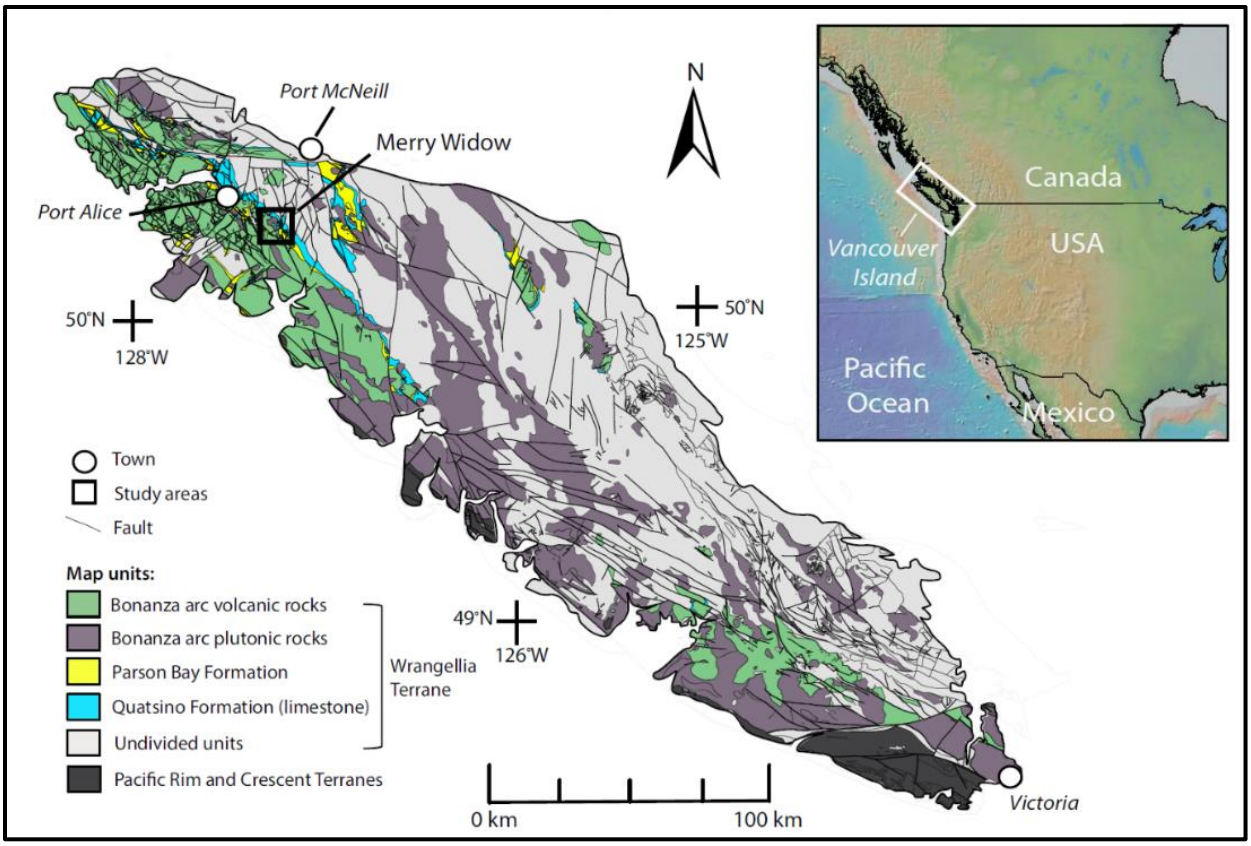

Figure 2: Regional geology of Vancouver Island, Canada. Study area is Merry Widow Mountain region highlight. Map displays the Jurassic Bonanza Arc volcanics intruding the underlying Triassic Quatsino Formation. The remaining Wrangellia terrains not labelled are represented as 'undivided units.' Image modified from Morris and Canil, 2022.

5. Geological and Petrographic Description

The contact of the Bonanza Arc volcanics and the underlying Quatsino limestone platform was directly sampled in outcrop in the Merry Widow Mountain region. Exposure of the contact was observed over a ~6 km strike-parallel section along the eastern slope of Merry Widow Mountain. Cross-cutting relationships were observed and show meter-scale dykes and sills (0.25 m to 2 m width) intruding the carbonate rock (Figure 3). In outcrop, the basaltic dykes show partial metamorphic alteration. The Triassic Quatsino limestone appeared as grey/white beds of micrite, that ranged from massive to bedded (Lund 1966; Ray and Webster 1991). The exposed limestone observed was <1 km thick and dipped at ~25^{o}-50^{o} southwest at the study location (Morris & Canil, 2019).

Cross-sectional profiles along the dyke-limestone contact were collected for study. Cut-rock slabs were made to form thin-sections for petrographic study (Figure 4 and Figure *5*). The thin sections show four distinct layers observed along the contact boundary which include: recrystallized limestone, skarn, boundary melt, and dyke interior. The presence of the skarn and boundary melt layers are indicative of the chemical reaction that has taken place between the limestone and melt.

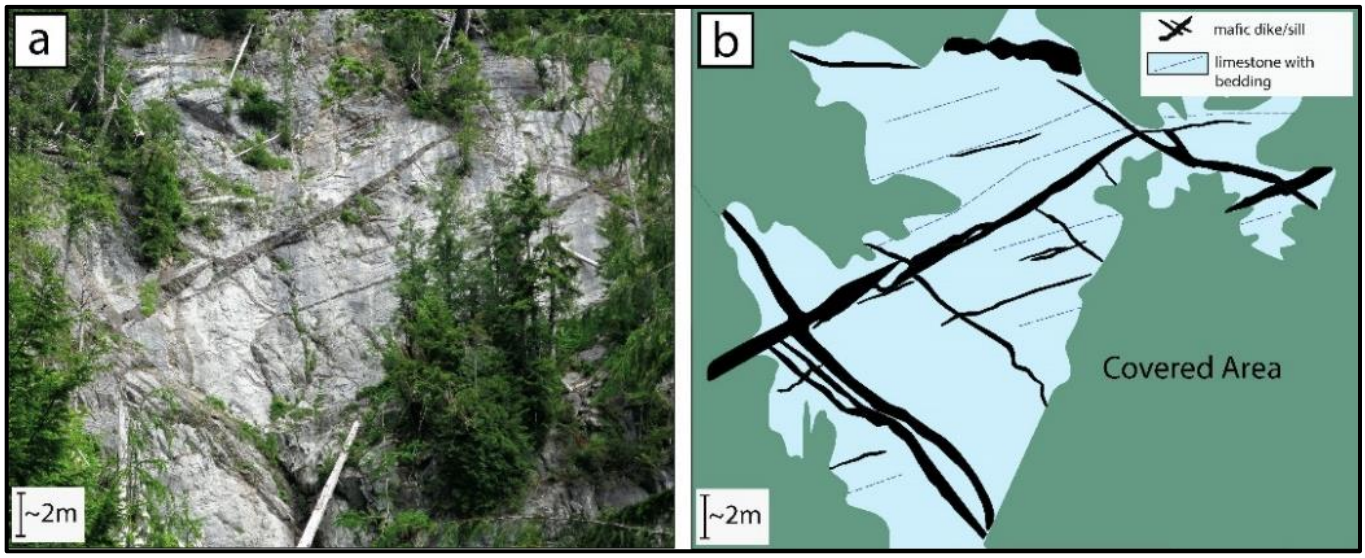

Figure 3: Outcrop photos taken from Merry Widow. Photos depicts the meter-scale dykes intruding the carbonate wallrock at the surface. Field photo taken by Morris & Canil, 2019.

A brief hand sample and petrographic analysis was conducted on the basaltic dykes to examine the primary mineralogy of the dykes and the overprint attributed by limestone assimilation. In hand sample, the dykes and sills are predominately aphanitic mafic rocks that ranged from aphyric to plagioclase-phyric. The primary mineralogy observed in thin section was plagioclase, clinopyroxene, oxides, and glass (Figure 5, photo D). The groundmass is fine-grained to hypocrystalline, with phenocrysts of plagioclase and clinopyroxene. Furthermore, there was extensive overprint by chlorite, epidote, actinolite, and albite which stained the dyke interior an olive-green colour in plain polarized light (PPL) (D). This secondary alteration was texture destructive and removed the primary crystallographic boundaries. Fractures were observed crosscutting the dyke interior that originated from the limestone contact. These fractures act as conduits for fluids which carry sulfide minerals (Figure 4). Subsequently, there is a low abundance of sulfide inclusions within the dyke interior that increase in modal percentage (1-3 %) as you move away from the boundary melt.

Moving towards the dyke-limestone contact, the next layer observed was the boundary melt (Figure 5, photo A). The boundary melt is a pale clay-grey colour in PPL and shows a meniscus (Figure 4). This meniscus is inferred to be the physical boundary between the limestone and dyke melt during mingling (Morris & Canil, 2022). Metasomatism has overprinted the boundary layer and destroyed all primary minerals within the original basalt. Fractures from the skarn boundary radiate into the boundary melt and carry sulfide minerals as blebs. Additionally, there is a trace abundance (<1%) of sulfide blebs which are coarsely disseminated within the boundary. Adjacent to the boundary melt is the skarn layer which appears as a bronze-brown layer in PPL. The skarn mineralization is composed of garnet, clinopyroxene, sulfides, and magnetite (B). The skarn exhibits high reflectivity due to pervasive sulfides scattered along the interface of the magma and limestone. The minerals display preferential elongation that is subparallel to the contact. Low-grade alteration is present as hematite staining and chlorite replacement on mafic minerals. Furthermore, the skarn layer is heavily fractured. These fractures are 0.02 mm in width and contain brownish-orange staining from metasomatism.

The final layer observed is the recrystallized limestone that is highlighted in photo C under cross polarized light (XPL) (Figure 5). Petrographically, the limestone contains medium-coarse equigranular grains of calcite. The limestone has experienced contact metamorphism and recrystallization as indicated by the granoblastic texture observed. There is a low abundance of sulfide minerals ranging from 0.01 – 0.04 mm in diameter with a coarse-disseminated texture.

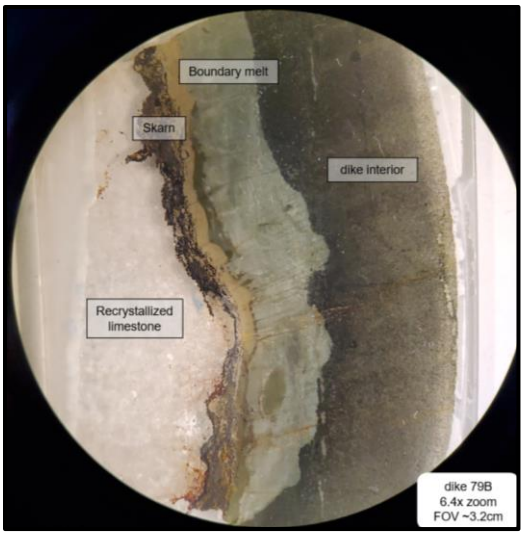

Figure 4: Macroscopic photo of dyke sample 79B in thin section. Cut rock slab is of the dyke-limestone contact at 6.4 zoom in plane light. Four distinct layers observed along contact: limestone, skarn, boundary melt, and dyke interior.

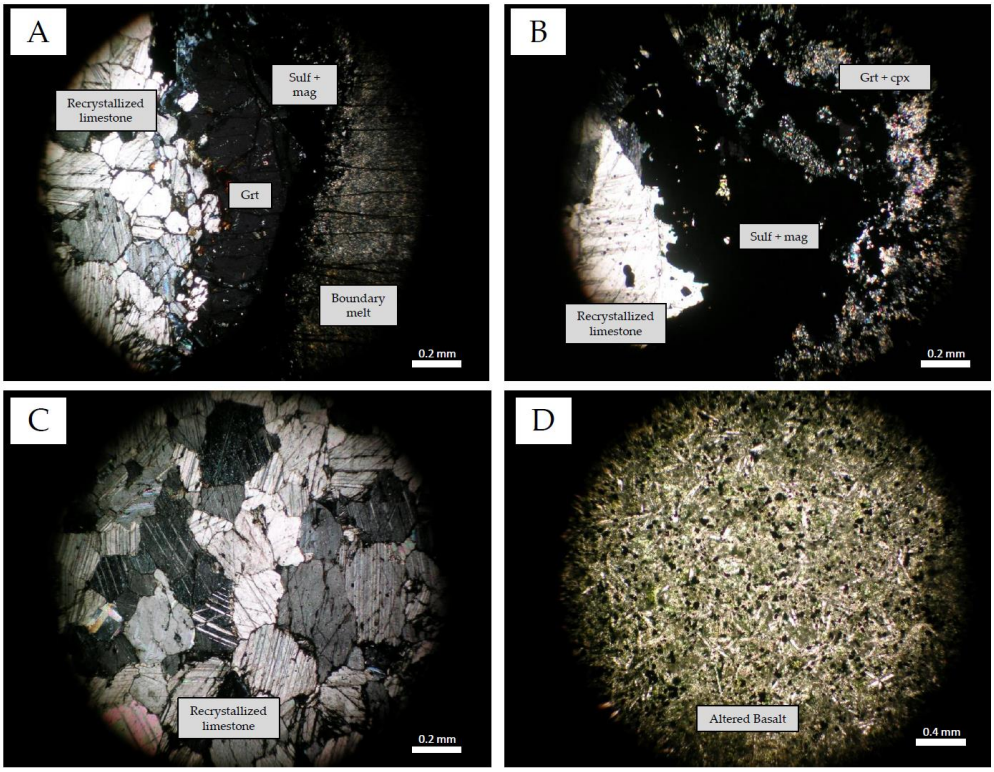

Figure 5: Petrographic images in both cross polarized light (A-C) and plain polarized light (D). (A and B) Photos depict the profile along the dyke-limestone contact. (B) Skarn mineralization composed of garnet, clinopyroxene, sulfides, and magnetite at the limestone contact in dyke sample 79B. (C) Microcrystalline limestone with granoblastic texture. (D) Microcrystalline basaltic interior melt composed of primary plagioclase, clinopyroxene, oxides, and glass. (D) Alteration overprint by chlorite, epidote, actinolite, and albite.

6. Methods

6.1. Dyke Samples

Two types of samples were investigated: (1) hand samples of dyke margins and interiors and (2) a single 25 cm cross-section of dyke #RM19-79B sampled at the milli-scale from margin to interior. Bulk rock powders of the dykes were prepared and analyzed for both major and trace element geochemistry. Bulk rock powders were made from the margin and interior of five dykes. For milli-slicing, the dyke #RM19-79B was cut into two rectangular sections, and then marked every 2.5 mm (Figure 6). The start of the intervals was adjacent to the skarn mineralization and moved into the interior of the dyke. Using a slow speed wet diamond saw, intervals one through five, and every 10th interval was cut out of the dyke as shown in Figure 6 to produce 14 milli-samples.

Figure 6: Twenty-five-centimetre (25 cm) cross-section of basaltic dyke 79B taken in-situ from Merry Widow Mountain. Sampled milli-slices one through ninety are labelled.

6.2. Glass Bead Preparation

Five pairs of dyke margins/interiors were powdered and prepped for fused-glass bead analysis (RM 19- 67A+B, 68A+B, 89A+B, 165A+B, 168A+B, and 70B). Dyke/sills in contact with the limestone are denoted as “dyke-in-limestone” and are represented by the letter “B”, while the interior of the dyke/sill has been labelled with the letter “A”. Each sample powder was mixed into a slurry with acetone in a ratio of 10:1, and then loaded onto a 0.15mm platinum (Pt) wire loop. The mixture was then sintered to the loop using a torch. For the milli-sliced sections, a chip of each slice was wrapped with a 0.15 mm Pt loop. The Pt loops with sample were pinned to the clothesline and fused at 1300 ^{o}C for 90 to 120 minutes. The Pt loop at the bottom provided sufficient surface area to allow the melt sample to rest on the hook via surface tension. After the fusion, the samples were removed from the furnace and quenched into glass

using an air stream. The glass beads were mounted in epoxy and polished with diamond grit until a fresh glass surface appeared for data analysis.

6.3. Data Collection and Processing

Dyke samples mounted in epoxy were analyzed using Laser Ablation Inductively Coupled Plasma Mass Spectrometer (LA-ICP-MS) at the University of Victoria. Data was collected for 42 masses. For the glass beads, the laser was configured to a repetition rate of 10 Hz and a fluence of 6.12 J/cm^2 to ablate a 100-micron diameter spot. The glass beads were ablated in raster mode along 300 µm lines at a scanning rate of 15 µm/sec for a total count time of 60 s. Prior to firing the laser, background count rates were measured for 30 s. The ablated sample material is introduced to the ICP in a stream of He and is ionized by the inductively coupled plasma, before being introduced to the mass spectrometer. The mass spectrometer segregates the ions by their mass-to-charge ratio and counted each ion to obtain an output data represent in “counts per second” for the ion stream.

To calibrate the LA-ICP-MS, three known standards were analyzed (BCR-2G, BHVO-2G, and KL2-G). Each standard was measured at the start, and then every 10th run during the data collection period. Sample standards BCR-2G and BHVO-2G acted as internal standards during the data collection process. Subsequently, standard BCR-2G was ablated every 10th analysis to track the drift of the instrument. Abundances collected from the external standard KL2-G were compared to their known values to determine data accuracy (Figure 8). The elements and their respective averaged detection limits (in ppm) include: ^{45}Sc (0.15), ^{51}V (0.05), ^{52}Cr (0.40), ^{59}Co (0.06), ^{60}Ni (0.34), ^{63}Cu (0.21), ^{93}Nb (<0.01), ^{85}Rb (0.04), ^{88}Sr (0.06), ^{232}Th (<0.01), ^{238}U(<0.01), ^{89}Y(<0.01), ^{90}Zr(<0.01), ^{137}Ba(0.07), ^{178}Hf (<0.01) as well as 14 rare earth elements (REE), all with detection limits <0.01 ppm with the exception of 153Eu (0.02) and 157Gd (0.05). Data was compiled and reduced at the University of Victoria using the IoliteTM (V4.8) software package (Paton et al., 2011).

6.4. Sr and Eu Anomaly

To help characterize the processes that may explain the changes in geochemistry of the basaltic dykes, Sr and Eu anomaly plots were constructed (Figure 15). Sr and Eu anomalies are empirical quantities that were calculated using the equations 1 and 2. Sr anomaly is the ratio of the observed Sr value to that predicted based on the abundance of two neighbouring trace elements with similar compatibility within the PUM normalized sequence (Pr and Nd). A visual representation of Sr anomaly is depicted in (Figure 7). Similarly, Eu anomaly is a ratio of the observed Eu to the predicted based on the elements Gd and Sm.

Sr anomaly calculation:

$$\frac{Sr}{Sr^*} = \frac{Sr_{obs}}{\sqrt{(Pr_{obs} * Nd_{obs})}} \qquad \text{(Equation 1)}$$

Eu anomaly calculation:

$$\frac{Eu}{Eu^*} = \frac{Eu_{obs}}{\sqrt{(Gd_{obs} * Sm_{obs})}} \qquad \text{(Equation 2)}$$

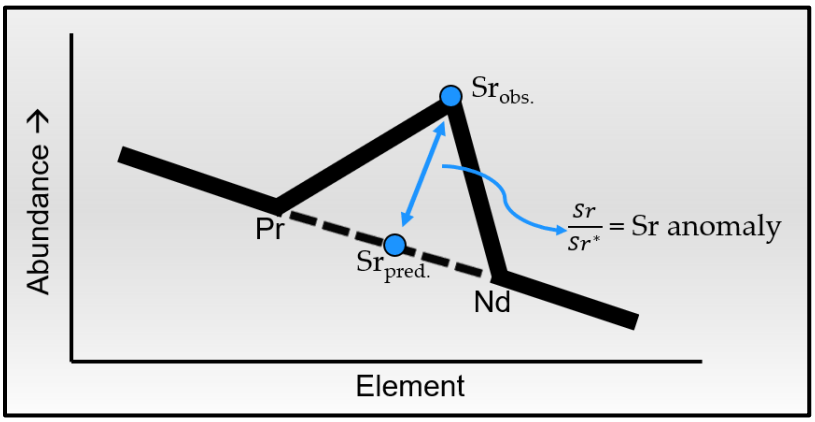

Figure 7: Schematic representation of the empirical Sr anomaly calculation. Sr anomaly is the ratio of the observed Sr value to that predicted based on the neighbouring trace elements Pr and Nd.

6.5. Calculating Sulfur Content at Sulfide Saturation

Sulfur content plays an important role in the formation of ore depositions. One way to characterize the maximum sulfur content a melt can dissolve is by empirically quantifying Sulfur Content at Sulfide Saturation (SCSS). SCSS was calculated using an empirical formula from O'Neill (2021) which uses the geochemistry of the magma. The controls on magma SCSS are pressure and the content of SiO_2, Al_2O_3, CaO, TiO_2, MnO, alkalies (Na_2O and K_2O), and total FeO. Constraints on pressure were estimated to be 0.1 GPa based on the emplacement (3 km) of the Bonanza Arc volcanics at Merry Widow (Canil and Morris, 2023). The calculated SCSS was plotted versus distance along the profile for dyke sample 79B (Figure 16).

7. Analytical Section

Percentage difference plots were generated to study the accuracy of the LA-ICP-MS data collected from the glass beads (Figure 8). There were two periods of data collection in which the external standard K2L-G was also measured alongside for accuracy. KL2-G trial runs one and two were gathered during the data collection process for the bulk dyke samples (Dec 2023), while trials three through five were taken during milli-slice collection period (Jan 2024). The measured geochemistry for K2L-G was contrasted against literature major and trace element abundances to produce the percent difference plots in Figure 8 (Jochum et al., 2005). Furthermore, a duplicate analysis of milli-slice interval #60 was gathered to examine the accuracy within the milli-slice profile. A third percent difference plot (Figure 9) was constructed using this duplicate milli-slice.

All three percent difference plots (Figure 8 and Figure 9) depict a similar distribution of error across the elements studied. All major and trace elements contain a deviation below +/- 30%, with most element errors below +/-10% from their literature value. For the KL2-G standard, the elements that carry the most inaccuracy are P, Zn, and Pb. Whereas the duplicate milli-slice data contains additional inaccuracy in Al, Si, Cr, Co, and Ni. These elements have been neglected for further data analysis as their precent error are too large to draw conclusive evidence from. Additionally, sufficient accuracy has been achieved in trace elements such as REEs and LILs (large ion lithophiles), as well as Fe and Mn. These elements have been used for further characterization of the dykes.

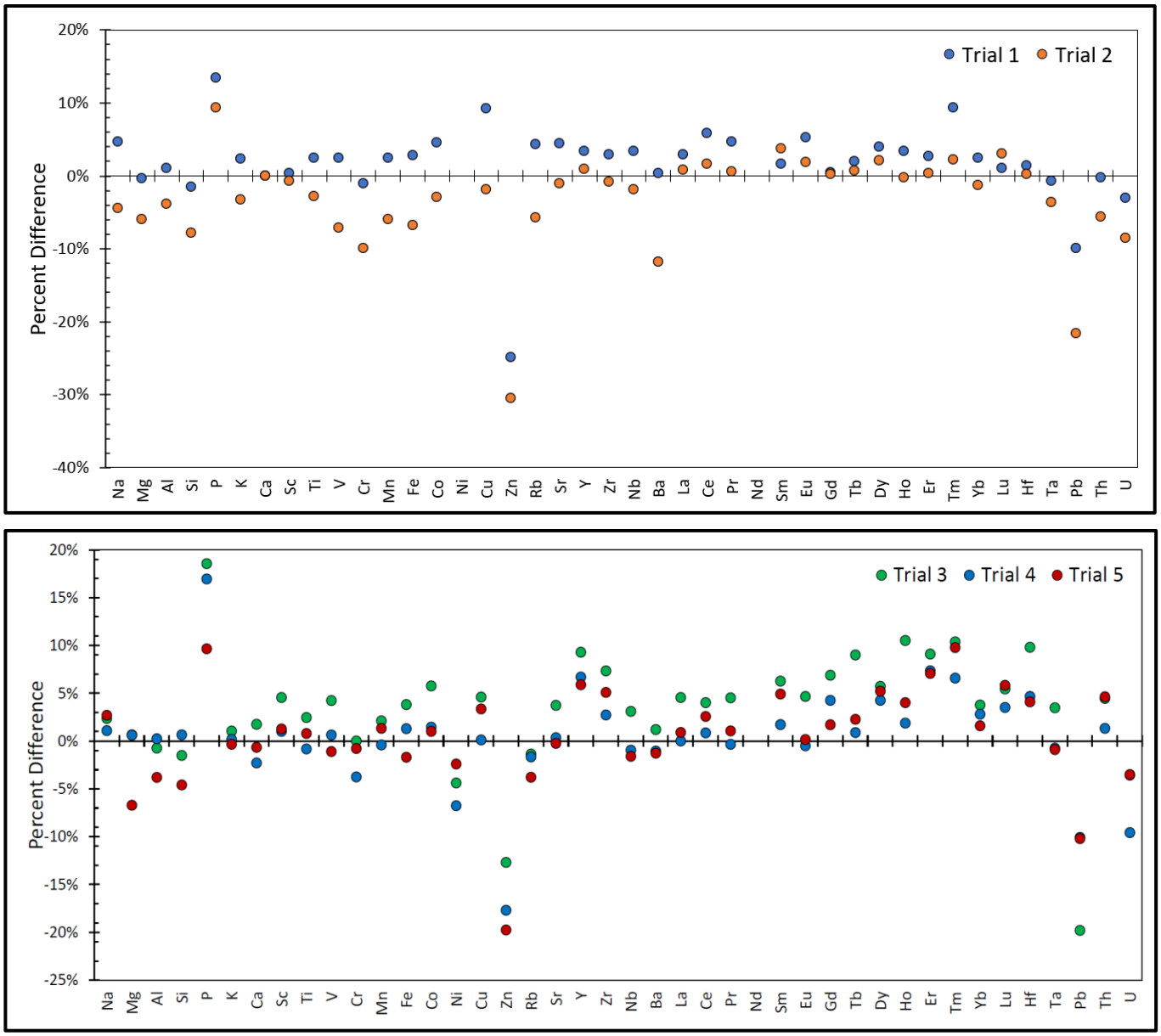

Figure 8: Percent difference plot for the observed elemental abundances collected from the external standard K2L-G using LA-ICP-MS. KL2-G trial runs 1 and 2 were gathered during the data collection process for the bulk dyke samples (Dec 2023), while trials 3-5 were taken during milli-slice collection period (Jan 2024). Trials were normalized using known elemental abundances for K2L-G (Jochum et al., 2005).

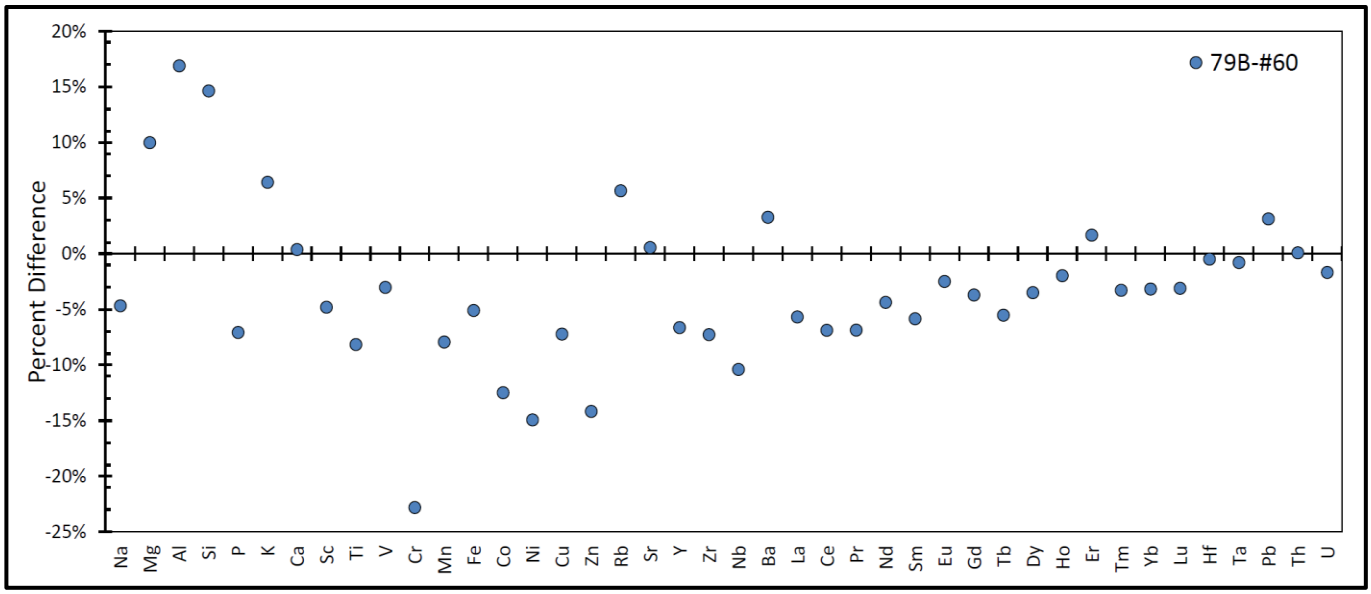

Figure 9: Percent difference plot for duplicate milli-slice interval #60 that was sampled from dyke 79B profile and analyzed using LA-ICP-MS. Milli-slice #60 was contrasted against the duplicate slice #60 to calculate percent difference.

8. Results

8.1. Dyke Geochemistry

Major and trace element geochemistry was collected on the Merry Widow dykes using LA-ICP-MS. The raw mean and limit of detection (LOD) for bulk dyke samples are summarized in Appendix 12.1 and the milli-slice profile summarized in Appendix 12.2. Subsequently, the external standard data for KL2-G and the duplicate milli-slice #60 are summarized in Appendix 12.3. Major element data is reported in weight percent (wt%) and trace elements in parts per million (ppm).

8.2. Dyke Comparison with PUM and Chondrite

Trace element data for the bulk dyke and milli-slice samples were normalized to primitive upper mantle (PUM) and chondrite (Figure 10 and Figure 11). The sample data was contrasted against a comprehensive database of Jurassic Bonanza Arc volcanic rocks, which are plotted as pale grey lines for comparison (Ray & Webster, 1991; Paulson, 2010; Morris & Canil, 2022).

For both the bulk dyke and milli-slices, the PUM plot data follows a similar pattern to that of typical Bonanza Arc volcanics, referred to as 'reference basalts' (Ray & Webster, 1991; Paulson, 2010; Morris & Canil, 2022). The trend reveals that all dyke data is enriched in every element relative to PUM, apart from V and Cu. This enrichment is highly variable, spanning over two orders of magnitude. There is a trend where all dyke samples are enriched in Sr, and either plot similar or above the reference basalts. The Sr enrichment is very pronounced in the milli-slice data with abundances over 100 times greater then PUM and 10 times the reference basalts. Conversely, all dyke samples carry negative Nb and Ti-oxide anomalies which is reflected in most of the reference Bonanza Arc data. Moreover, there's also a slight negative anomaly reported for Pb across the dyke data, but this is only partially reflected in the reference basalt data. Across the suite of dyke data, there is a high variability in the degree of enrichment across both the bulk dyke and milli-slice samples. However, for a select few elements like Pb, Sr, and Ti-oxide, the milli-slices report a high precision with one another. This precision is not mirrored in the bulk dyke samples. Observations between each pair of bulk dyke samples shows no correlation whether the dyke interior is more enriched than its complimentary margin value. Similarly, there is little

correlation in geochemical results across the dyke profile. The milli-slices closest to the limestone contact do not show drastically different geochemical signatures compared to the outer-most slices.

Chondrite plots for both the bulk dyke samples and milli-slices are contrasted against Bonanza Arc data for comparison (Figure 11). Initial observations shows that all the sampled dyke data depicts a strong correlation with the reference basalt data (Ray & Webster, 1991; Paulson, 2010; Morris & Canil, 2022). All basalts carry the characteristic decrease in abundance moving from the LREEs to the HREEs and all are enriched in REEs relative to chondrite. There is an equal spread where half the bulk dyke data matches typical Bonanza Arc volcanics and the other half is slightly over-enriched in every REE. There is no correlation whether the dyke margin is enriched or depleted in relation to its dyke interior. Conversely, the milli-slice data reported less deviation between one another. The milli-slices adjacent to the limestone contact generally reported lower enrichment values when contrasted against the inner-most milli-slices. Individual element observations show that all dyke samples and the reference basalt data carry an anomaly for Eu. This Eu anomaly is mostly negative across the dyke samples with the exception for bulk dyke samples 165B, 67A+B, and milli-slices 10.7 cm, 18.9 cm, and 21.5 cm.

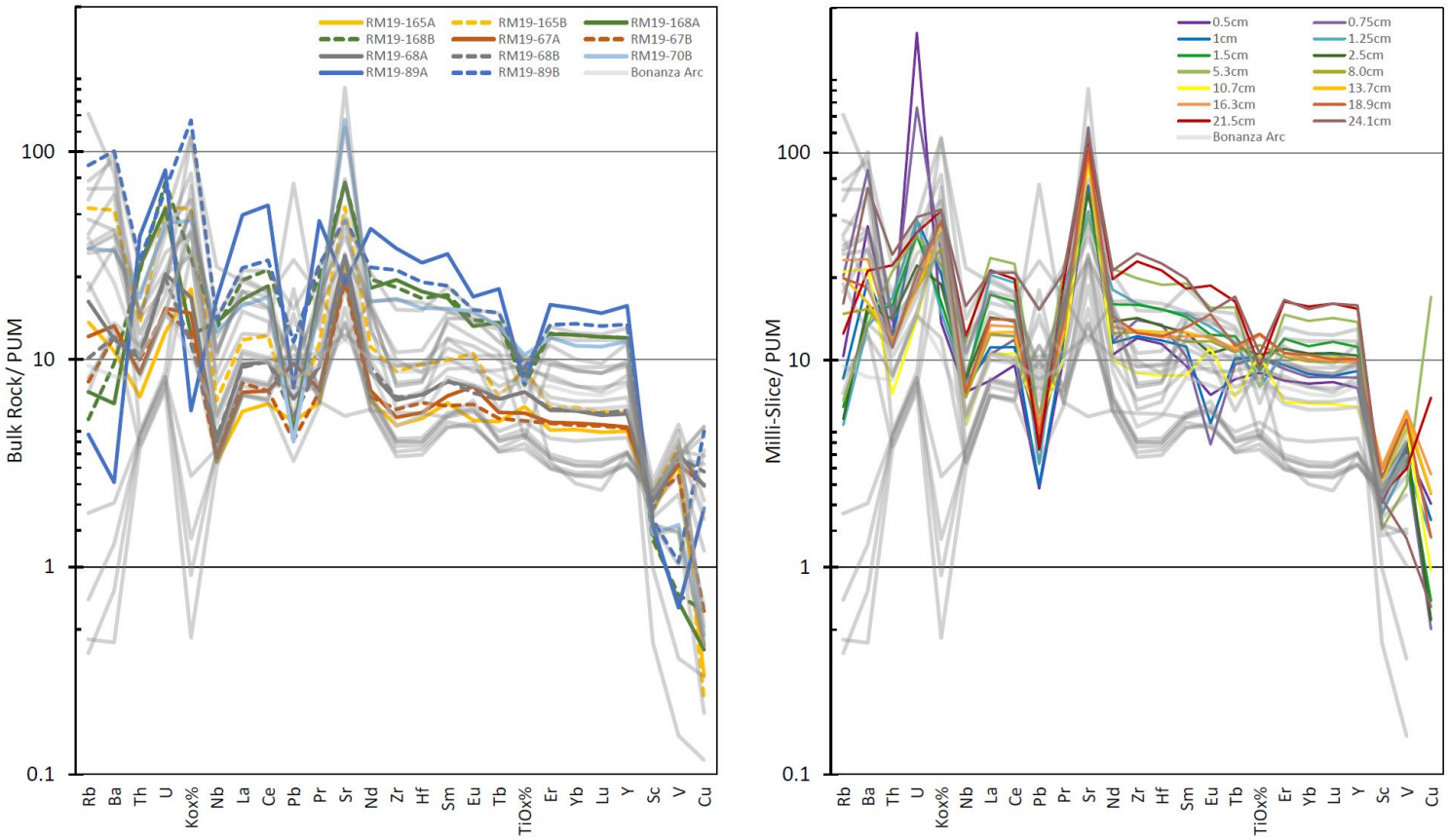

Figure 10: Normalized PUM plots for the bulk dyke and milli-slice data contrasted against typical Bonanza Arc volcanics. The reference Bonanza Arc data is represented as pale grey lines with the taken from Ray & Webster, 1991; Paulson, 2010; and Morris & Canil, 2022.

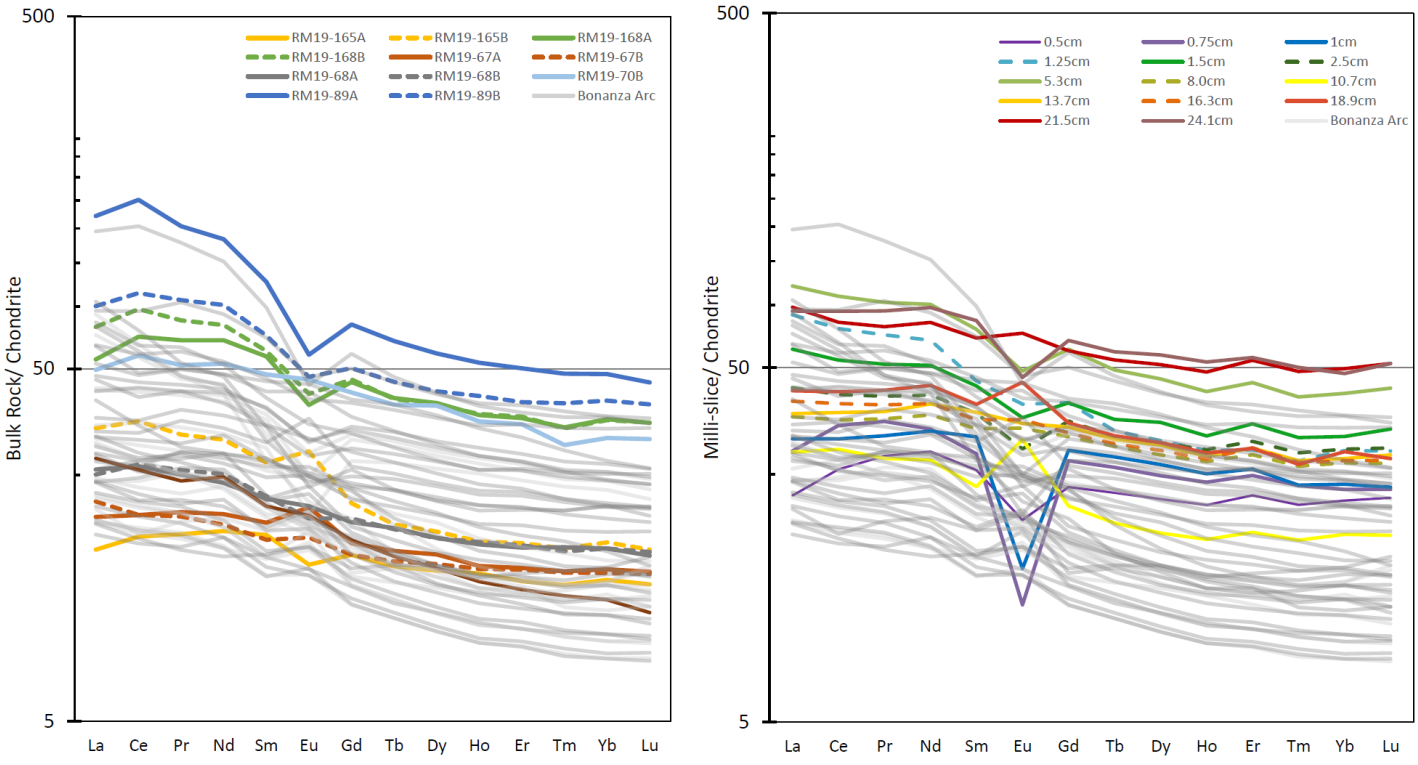

Figure 11: Normalized Chondrite plots for the bulk dyke and milli-slice data contrasted against typical Bonanza Arc volcanics. The reference Bonanza Arc data is represented as pale grey lines with the taken from Ray & Webster, 1991; Paulson, 2010; and Morris & Canil, 2022.

To characterize the magnitude of enrichment across the reacted dykes, each dyke margin was normalized to its complementary interior pair (Figure 12). Normalized elemental ratios above one represents the margin of the dyke being over enriched in comparison to the dyke interior. Whereas a value of one represents no enrichment at the margin for the specified element when it reacted with wallrock limestone. Dyke pairs #67, 68, 165, and 165 show a rather constant ratio of one between the dyke margin and interior. Dyke pair 165 slightly deviates for the heavier trace elements as seen by the enriched margin values for Rb, Ba, U. All dyke pairs report either a positive or negative anomaly with the element Pb. This data is exempted as Pb has been previously determined to be inaccurate based on the external standard examined. Furthermore, dyke 168 shows an unpredictable enrichment profile. The margin of dyke 168 appears super-enriched in LILs like K_2O, Rb, and Ba and heavy depleted in other elements such as Ni and La. Moreover, the normalized ratios observed in dyke 168 are much more pronounced than in the other four dyke pairs. General trends in the dyke pairs shows that most dyke pairs carry enrichments in LILs and no enrichment for the REEs.

To further explore the enrichment of these dyke pairs in LILs, normalized bivariant plots were constructed (Figure 13). Each dyke margin was normalized to its complimentary interior. The plots depict a positive correlation between K with the LILs of Ba and Rb. Dyke pairs 68B, 67B, 168B, and 165B reported either no enrichment or a very minor enrichment pattern above their interior counterpart. Furthermore, these dyke pairs contain a low deviation between one another. Conversely, dyke pair 89B carries an anomalously high enrichment ranging from 20 to 40 times greater when compared to its interior value. As such, dyke pair 89B reports a very different LIL signal compared to the other dyke pairs sampled.

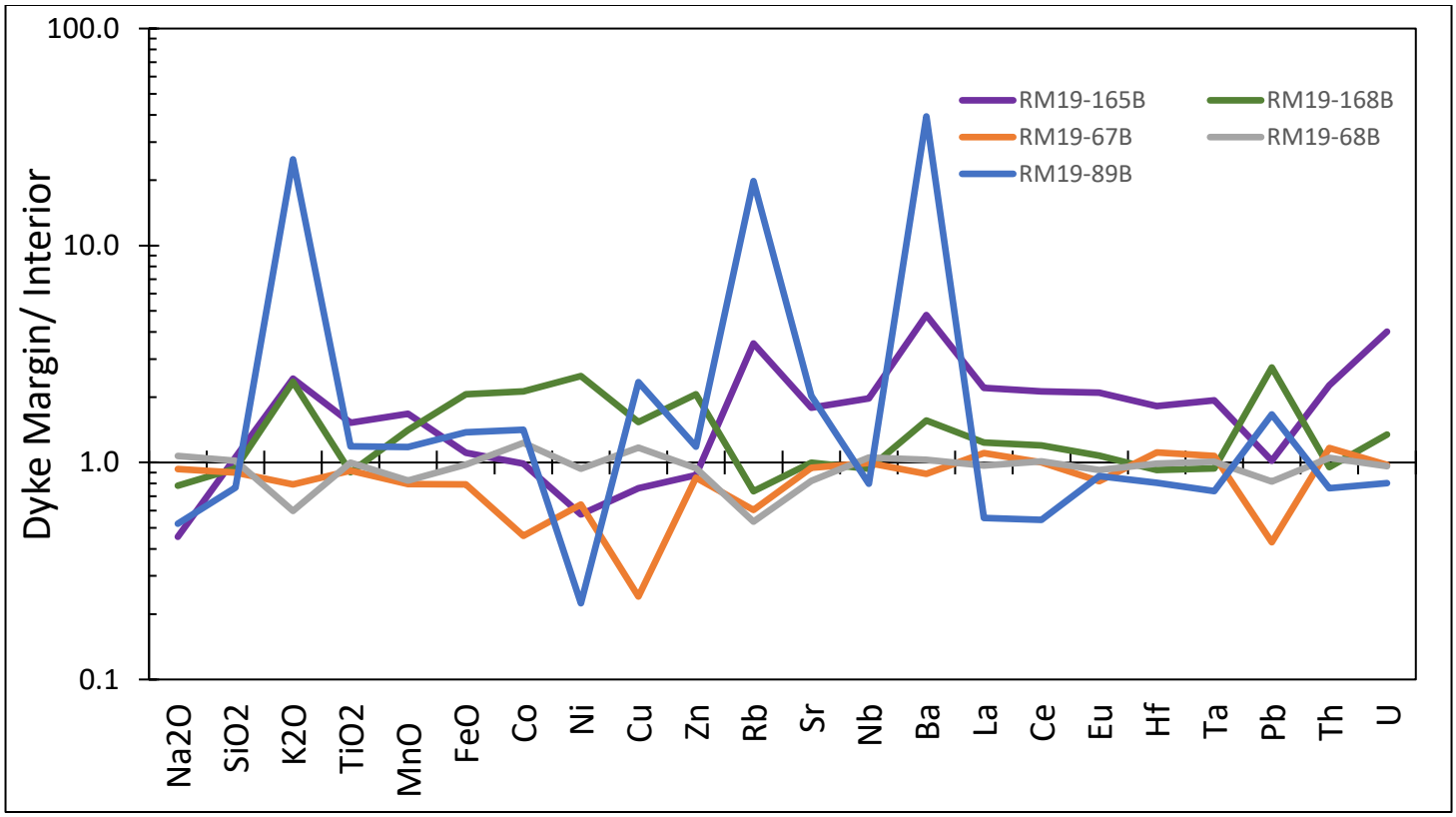

Figure 12: Geochemical enrichment plot for the bulk dyke margin samples. Margin samples were normalized to their complimentary dyke interior sample. Elements with a value >1 indicate an enrichment in the dyke margin, relative to the dyke interior, whereas values <1 show depletion in the margin.

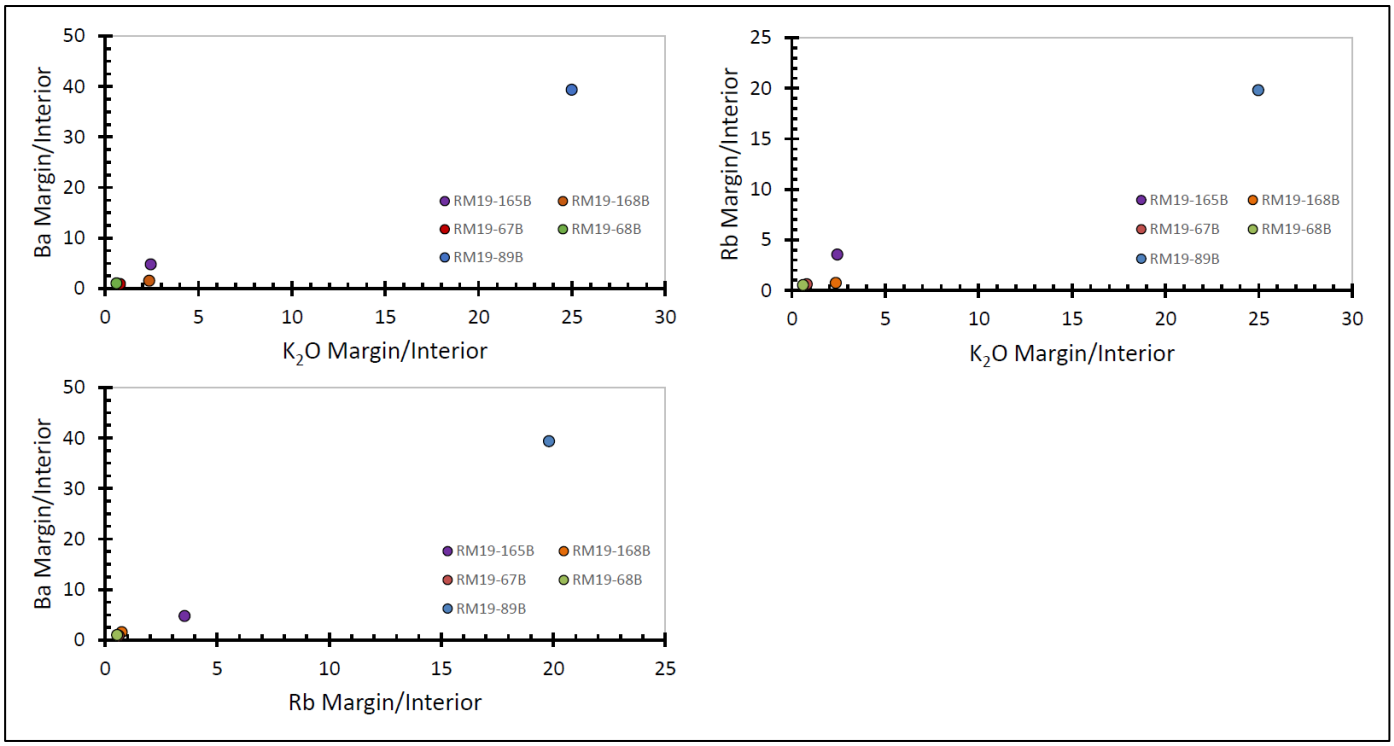

Figure 13: Bivariant plots constructed for the elements of K, Ba, and Rb within the bulk dyke samples. Each dyke margin was normalized it its complimentary interior value. A positive correlation in the data depicts a relationship between the abundances in the two elements.

8.3. Geochemical enrichment along the dyke profile

Geochemical profiles for select major (MnO, Na_2O) and trace elements (Rb, Sr, U) were constructed to study the distribution of elements along dyke sample 79B (Figure 14). Milli-slices start adjacent to the limestone contact at 0.5 cm and increase in distance towards the dyke interior. There is a high variability between enrichment plots with Na_2O depicting an increasing abundance towards the dyke interior. Whereas U and MnO demonstrate a declining trend, and the LILs of Rb and Sr, report a more complex distribution. Within the Na_2O plot, the abundance of Na_2O steady increases from 0.35 wt% adjacent to the limestone contact with milli-slices 0.5 cm – 1.5 cm, before plateauing at ~4 wt% in the middle of the dyke profile. Furthermore, Na_2O abundance increases in the last three milli-slices to a maximum of 9.3 wt%. Conversely, MnO depicts an inverted distribution to Na_2O with a rapid decrease in abundance from 0.46 wt% at the contact, a similar stagnation at 0.26 wt% within the intermediate milli-slices, and a final decline to a minimum value of 0.20 wt% within the dyke interior. The plateauing trend in both Na_2O and MnO appears within the same milli-slices (2.5 cm to 18.9 cm). The U enrichment plot shows a maximum of 8 ppm adjacent to the limestone contact, and then rapidly decreases to 1 ppm as you move into the dyke interior.

The enrichment plots of Rb, and Sr do not report a linear change in trace element chemistry, but rather a sinusoidal distribution. These two enrichment plots report two maximum values throughout the profile, one near the LST contact and another towards the dyke interior. Interestingly for both Rb and Sr plots, their local maximum abundance is in milli-slice 0.75 cm (at 15 ppm and 2645 ppm respectively), not in slice 0.5 cm that is immediately adjacent to the LST contact. Subsequently, this local maximum value rapidly declines for both elements moving into the dyke interior. Despite similar compatibility between Rb and Sr in basalts, these two elements don't entirely mirror one another along the dyke profile. Rb's maximum abundance is in milli-slice 16.3 cm (at 18.2 ppm), not in milli-slice 0.75 cm like in Sr. Furthermore, Rb's maximum value declines as you move into the dyke interior. Comparatively, the Sr plot depicts a gradual increasing trend from milli-slice 8 cm to a local maximum value of 2,459 ppm in the last milli-slice. Finally, the Sr plot depicts super-enriched Sr abundances that range from 995 ppm to 2,645 ppm. These Sr values greatly exceed the reference basalts and limestone endmember compositions which is puzzling. Other studies have also reported highly enriched Sr values reaching 2,000 ppm Sr in altered mafic rocks (Natale et al., 2023). This predicament is further explored by studying the Sr distribution to infer a process that may explain this observed over enrichment.

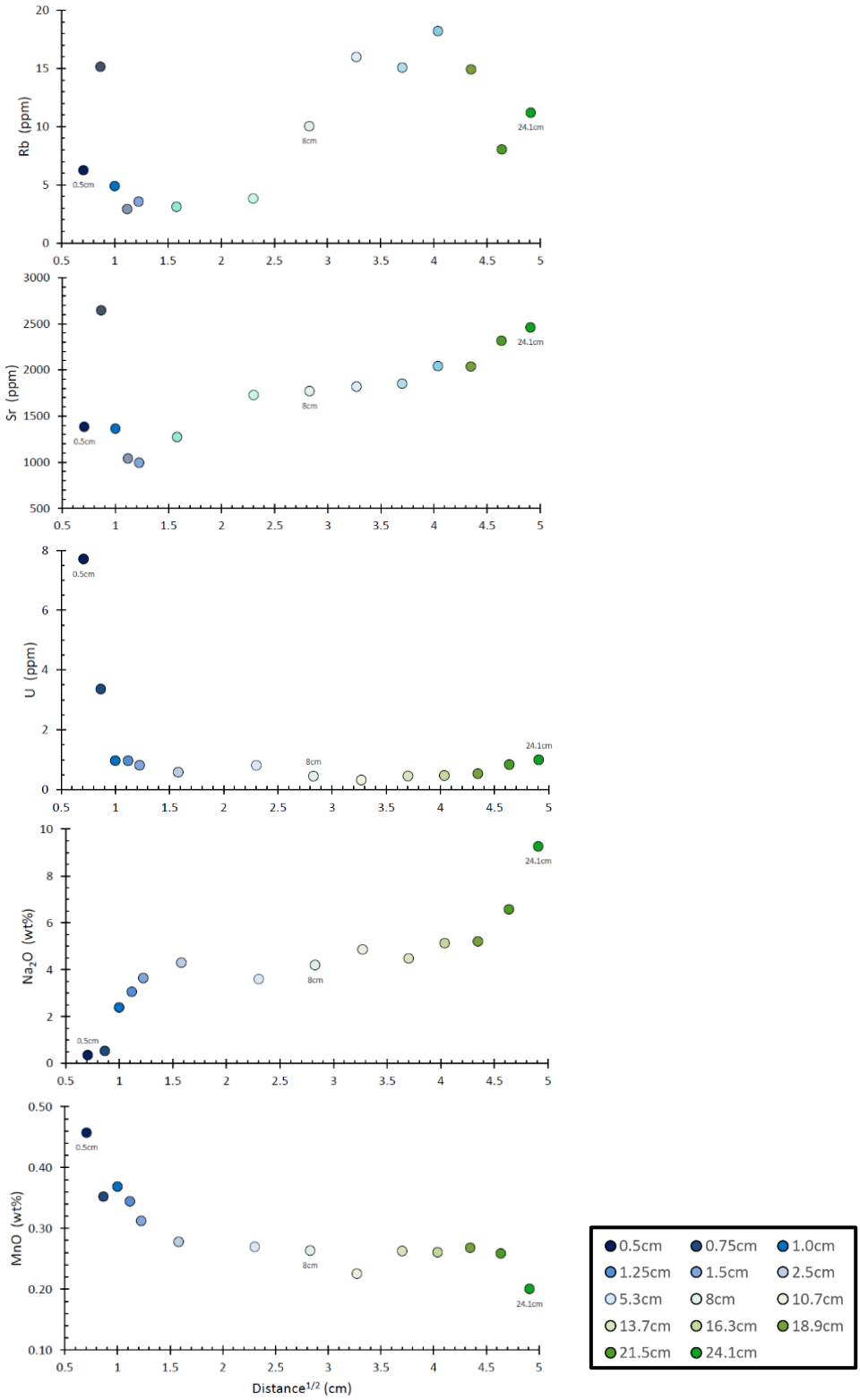

Figure 14: Select major and trace element abundances versus distance along a profile of dyke sample 79B. Milli-slice samples were taken adjacent to the limestone contact and increase in distance towards the dyke interior. Plots depict variability in the concentrations of Rb, Sr, U, Na_2O and MnO with distance.

8.1. A Process for Sr Enrichment

The PUM and chondrite plots depict strong positive Sr anomalies and negative Eu anomalies for the dyke samples. One way to explain these anomalous trends in Sr and Eu is by studying trace element partitioning within minerals. For example, U and Sr is compatible within calcite in carbonate rocks so limestone can achieve Sr values upwards of 6,000 ppm when it is deposited in shallow-marine environments like the Bahamas (Higgins et al., 2018, Kahle, 1965). For basaltic rocks, we can scrutinize the mineral plagioclase to help characterize the anomalous trends in both Sr and Eu using their empirical anomaly values, Sr/Sr* and Eu/Su*. This is because plagioclase fractionation or its accumulation will always create a positive correlation with both Sr and Eu anomaly (Dygert et al., 2020; Weill and Drake, 1973).

Sr and Eu anomaly plots were constructed to examine the distribution along the dyke profile (Figure 15). As observed, there is no clear trend in the plotted data, and these plots do not mirror one another. As expected, the Sr anomaly plot (Sr/Sr*) is analogous to the absolute concentration of Sr that is plotted in Figure 14 because of how Sr anomaly is computed. Sr anomaly depicts a sinusoidal pattern with a maximum of 10.6 in the second milli-slice and a local maximum of 9.1 in milli-slice 10.7 cm. Minimum values of Sr anomaly are observed near the dyke contact in milli-slices 1.25 cm to 5.3 cm.

The Eu anomaly plot (Eu/Eu*) contains values ranging from 0.4 to 1.5 with a medium value of 1.0. There is only one maximum value of Eu anomaly at 1.45 in milli-slice 10.3 cm. This is the same milli-slice sample for the local maximum seen in Sr anomaly. Furthermore, there is a slight depletion in Eu anomaly within samples 0.75 cm and 1.0 cm. The last three mill-slices in the dyke interior carry a declining trend. A Sr versus Eu anomaly plot was constructed to further compare these geochemical signatures within the milli-slice profile (Figure 17).

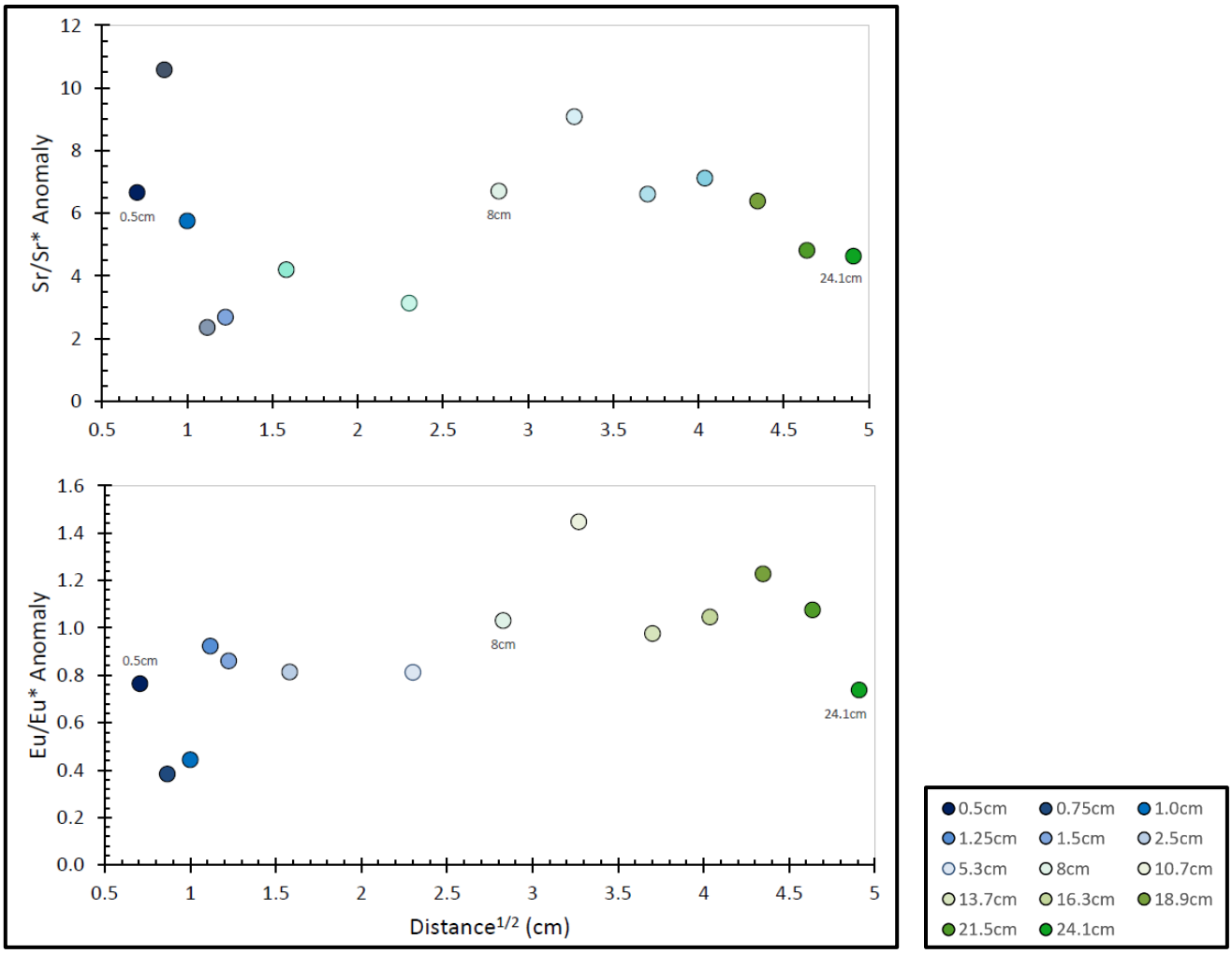

Figure 15: Calculated Sr and Eu anomaly versus distance along a profile of dyke sample 79B. Milli-slice samples were taken adjacent to the limestone contact and increase in distance towards the dyke interior.

8.2. Sulfide Saturation along Dyke Profile

A plot of SCSS versus distance along dyke sample 79B was created (Figure 16). The maximum SCSS is 2,080 ppm within the milli-slices adjacent to the limestone contact. The SCSS depletes into the interior of the dyke with a minimum value of 732 ppm reported 24.1 cm from the limestone contact. As such, the sulfur saturation limit is three times higher at the limestone contact than the dyke interior. The main controlling factors impacting the SCSS calculations are silica and CaO content. The reported content for the dyke margin was ~37 wt% silica and ~20 wt% CaO, whereas the milli-slices within the dyke interior report ~52 wt% silica and ~12 wt% CaO.

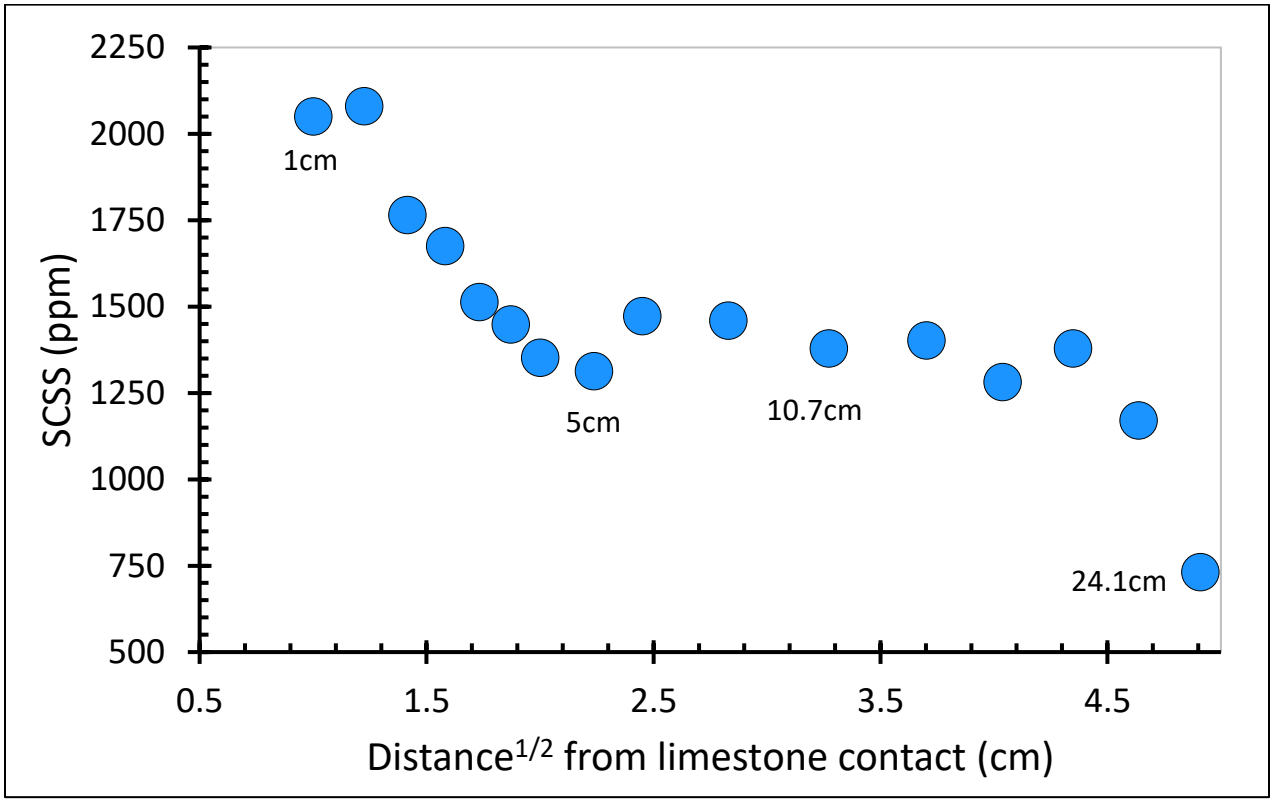

Figure 16: Calculated sulfur content at sulfide saturation verse distance along dyke 79B. Samples were taken adjacent to the limestone contact and increase in distance towards the dyke interior.

9. Discussion

9.1. Testing limestone assimilation as a process

As mentioned previously, the dykes possess unique geochemical enrichments in Rb, Sr, U, Na_2O and MnO. We can query these enrichment patterns using mineral fractionation to study whether the geochemistry results are due to a change in dyke mineralogy. The primary trace elements of concern were Sr and Eu because these two elements displayed anomalous abundances when compared to PUM and chondrite (Figure 10 and Figure 11). The basic mineralogy of the sampled dykes consists of olivine, pyroxene (clinopyroxene and orthopyroxene), and plagioclase feldspar. Both Sr and Eu are incompatible in all these mafic minerals except for plagioclase. Therefore, we can scrutinize the mineral plagioclase to determine if the trends in Sr and Eu are caused by mineralogical changes or by another process such as limestone assimilation. This examination was carried out by plotting Sr anomaly versus Eu anomaly (Figure 17). Within the plot, the bulk dyke samples are represented as triangles and the milli-slices as circles. Dyke samples have been contrasted against reference Bonanza Arc volcanics which are depicted as grey circles (Ray & Webster, 1991; Paulson, 2010; Morris & Canil, 2022). Additionally, the inferred enrichment process of limestone assimilation and plagioclase control have been added as red and black arrows respectively.

As illustrated, the reference basalt data generally plots along the plagioclase control line. This correlation is because Sr and Eu are both compatible within the plagioclase lattice, so their abundance is governed by the mineral's accumulation and depletion (Dygert et al., 2020; Weill and Drake, 1973). Therefore, plagioclase accumulation will always create a positive correlation between these two trace elements. Conversely, the positive trend of Sr and Eu anomalies is not reflected in either the bulk dyke or milli-slice samples. Instead, the sampled dykes plot along a unique-linear distribution with highly variable Eu anomalies and near constant Sr anomalies (2.4- 10.6). Notably, slices taken adjacent to the limestone contact report slightly lower Eu anomaly values which is consistent with the degree of partial mixing with limestone (Tanaka et al., 2003). Limestone carries a moderate, negative Eu anomaly because its mineral assemblage is entirely $CaCO_3$. As such, the milli-slices that carry the most depleted Eu anomalies can be linked to increasing mixing with limestone rock.

The increased Sr anomaly values within the dyke samples can also be attributed to partial mixing with limestone. As observed by the four Quatsino limestone sampled plotted, limestone reports very large Sr anomalies (Morris & Canil, 2019). We can infer that mixing of typical Bonanza Arc rocks with this highly enriched Sr in the Quatsino limestone, could result in the geochemical pattern seen by the sampled dykes. Furthermore, the degree at which these dykes have assimilated carbonate wallrock can be explored further using a mixing equation.

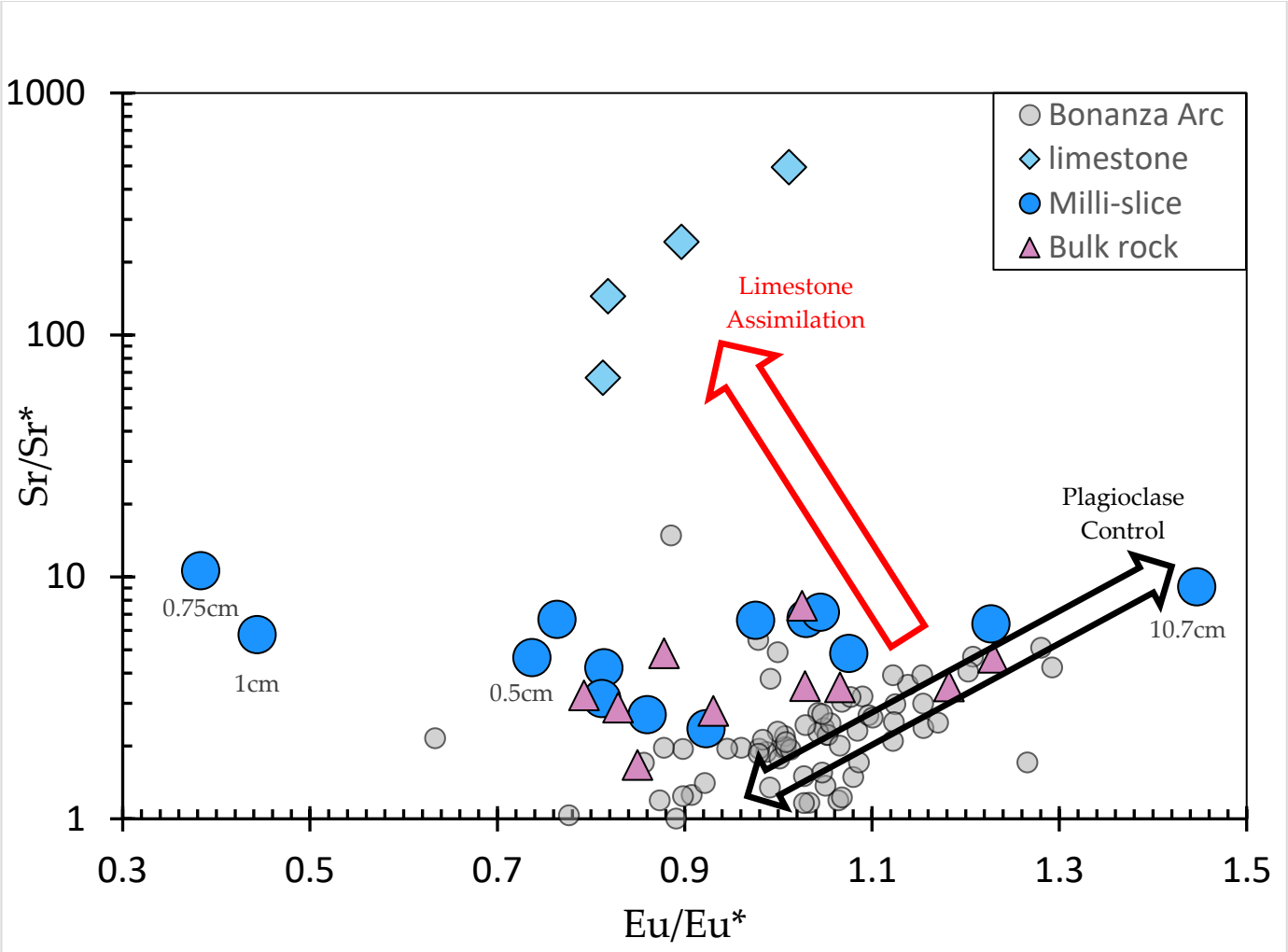

Figure 17: Plot depicts Sr vs Eu anomaly for the bulk dyke and milli-slice samples, contrasted against limestone and Bonanza Arc data. The milli-slice distance from the limestone contact has been provided for select samples. Bonanza Arc volcanics are represented as pale grey circles and the data was taken from Ray & Webster, 1991; Paulson, 2010; and Morris & Canil, 2022. The Quatsino limestone data was taken from Morris & Canil, 2019. The black arrow shows correlation by plagioclase control while the red arrow is correlation with limestone assimilation.

9.2. Degree of limestone assimilation

We can study the degree of limestone assimilation into basaltic melt as a process to describe the super-enriched Sr values observed within the dykes. This is completed using a binary mixing plot using Bonanza Arc basalt and Quatsino limestone as end-member compositions (Figure 18) (Morris & Canil, 2022). This plot can be generated with the assumption that these two components are the only contributors to the Sr composition observed in the dykes (Faure, 1997).

The initial assumptions for the mixing plot were a maximum Sr value of 650 ppm for Bonanza Arc basalt, and an average Sr value of 720 ppm for the Quatsino limestone (Morris & Canil 2022). A mixing line, represented as a dash line, was plotted between these two endmember compositions. Noticeably, the dyke samples do not plot along this original mixing line, but rather along a separate mixing profile with a different limestone composition referred to as a "theoretical" or "assumed" limestone. The existence of the assumed limestone can be reinforced because the dyke samples plot off the original mixing line which indicates contamination with a third component (Faure, 1997). The inferred Sr value for the theoretical limestone was chosen to be 10,000 ppm based on Sr values observed in modern-day carbonate rocks (Kahle, 1965; Higgins et al., 2018). If a lower Sr value was chosen, such as 6,000 ppm, more assimilation would be required to produce the desired concentration in the dyke samples. Following the burial and cementation of limestone, carbonate rocks quickly undergo diagenesis which can cause its Sr content to be altered (Higgins et al., 2018). The process of lithification could indicate why the Quatsino limestone sampled at site does not report super-enriched Sr values. Furthermore, we can infer that the enriched Sr in the dykes is from the result of assimilation by a theoretical limestone prior to or during diagenesis.

The mixing calculations highlight that the milli-slice samples require between 30 wt% to 80 wt% assimilation of a theoretical limestone, into basaltic melt to explain the super-enriched Sr values of 2,400 ppm Sr observed in the dykes. This degree of assimilation is questionably very high, especially when considering that assimilation is controlled by a thermal barrier as melts transition from silica-saturated to silica-undersaturated (Watkinson and Wyllie, 1969; Iacono Marziano et al., 2008). However, this thermal barrier is relegated to the vicinity of the sidewall around a magma chamber and therefore prevents adequate mixing within the chamber to accommodate more assimilation (Iacono Marziano et al., 2008). As such, the degree of assimilation is more governed by the surface area along which magma is in contact with limestone, compared to the volume of the magma itself. Furthermore, volume constraints along the contact region are absent because the reaction generates CO_2 which is removed from the

system by rapid degassing (Barnes et al., 2005; Carter and Dasgupta, 2016). It can be said that dykes and sills carry a much larger surface area to volume ratio than typical plutonic bodies. This would therefore allow dykes to accommodate much higher degrees of limestone assimilation during their emplacement into carbonate rock. The increased surface area of the Bonanza Arc dykes allows for more efficient mixing with carbonate rock and therefore promote assimilation of up to 80 wt% as observed in the dyke data.

Another particular interest of limestone assimilation is the production of volcanic CO_2 that originates within the arc crust. The process by which CO_2 is degassed from the melt during the assimilation process is characterized in equation 3 where carbonate rock is partially melted by silica-rich melt (Xu et al., 2023). The constraints on equation 3 is only limited by the supply of magma, mixing constrains, and the thermal budget required to melt the carbonate rock (Morris et al., 2023; Xu et al., 2023). With basaltic rocks containing silica content ranging from 41-57 wt%, there can be a high degree of limestone assimilation that would cause desilication of the melt and intense decarbonation. Estimates for CO_2 production can be calculated knowing that typical limestone rocks contain ~44 wt% CO_2. Using the binary mixing model results, assimilation of between 30-80 wt% limestone into basalt is capable of degassing ~13-35 wt% CO_2 within the dyke profile. As such, shallow crustal assimilation is an effective mechanism to produce profound amounts of CO_2 from arc magmas.

$$CaCO_{3(limestone)} + SiO_{2(melt)} = CaSiO_{3(melt)} + CO_{2(gas)} \qquad \text{(Equation 3)}$$

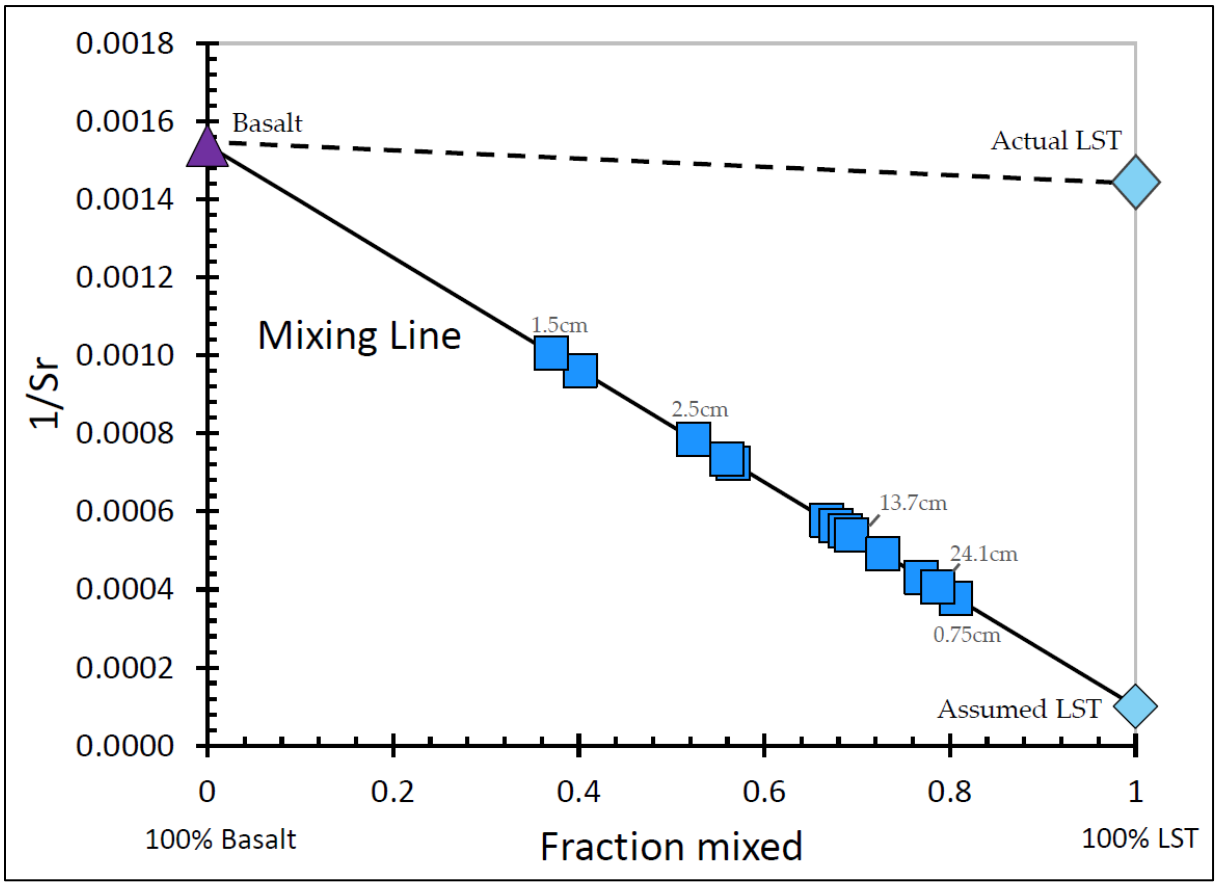

Figure 18: Binary mixing plot for the Sr content between the endmembers, Jurassic Bonanza Arc basalt and Quatsino Limestone. The limestone is sampled at Merry Widow study area is represented as "actual LST" and the theoretical limestone used for mixing calculated is denoted as "assumed LST." The milli-slice samples from dyke 79B are represent as squares along the mixing line. The assumed endmember Sr compositions for BAS and assumed LST were 650 ppm and 10,000 ppm respectively (Morris & Canil, 2022).

9.3. Sulfur Transport within Dykes

Another important product of magma-carbonate interacting is the affects on sulfur saturation. Sulfur species plays two important roles within the geosphere (D'Souza & Canil, 2018). Dissolved sulfur in magma can form an immiscible sulfide phase and assist in the partitioning of chalcophile elements like Cu, Pb, Zn out of a silica-rich melt (D'Souza & Canil, 2018; Zelenski et al., 2018). This partitioning is a crucial process to the transport and concentration of base metals for ore deposition. In addition, once sulfur is finally degassed into the atmosphere at volcanic arcs, the H_2S and SO_2 products impact global climate (McLinden et al. 2016).

The capacity of a melt to dissolve sulfur is known as Sulfur Content at Sulfide Saturation (SCSS). Quantifying SCSS is important because it governs the quantity of sulfur that can be dissolved within a magma body. SCSS is calculated based on the known geochemistry of a melt and its depth of emplacement (O'Neill, 2021). The main contributors to the sulfide saturation are silica content, CaO content, temperature, and the fO_2 of the melt (D'Souza & Canil, 2018; O'Neill, 2021). Temperature and fO_2 are constrained using the total Fe abundance and trace element chemistry of Ni and Cu (O'Neill, 2021). As illustrated in the SCSS versus distance plot (Figure 16), the profile along dyke 79B records a decreasing trend in sulfur saturation from 2,080 ppm to 732 ppm. The declining trend is primarily imputable to changing silica and CaO content along the dyke profile. Between the dyke margin and the interior, the milli-slice adjacent to the limestone contact reported ~15 wt% less silica content and 8 wt% more CaO. These changes in the dyke chemistry are inferred to be caused by limestone contamination which causes both desilication, a decrease silica content, and CaO enrichment within dykes (Barnes et al., 2005; Carter and Dasgupta, 2016; Iacono Marziano et al., 2008). However, because assimilation is restricted to the peripheral margin of a magma body, only the milli-slices neighboring the limestone contact will induce this chemical change, while the interior milli-slices will remain silica-saturated (Iacono Marziano et al., 2008). The net result is the margin of the dykes containing a higher SCSS and thereby a greater capacity to transport sulfur species.

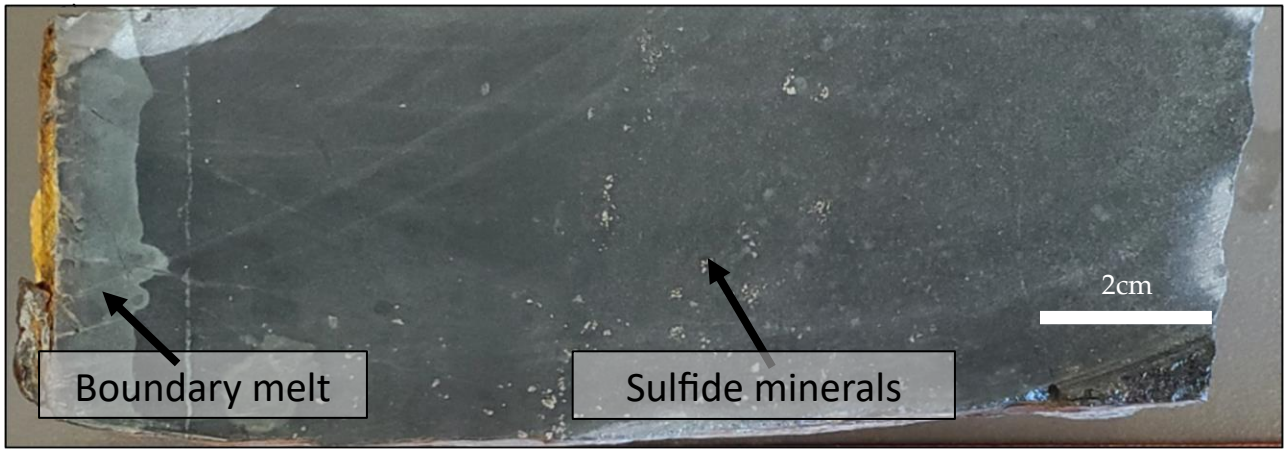

Figure 19: Cut rock slab sample along a 13 cm cross section of sill 58B. Distance is measured adjacent to the limestone contact and increases towards the dyke interior. Visible sulfide minerals are present within the sill interior.

A modern analogue that describes how SCSS changes in a dyke melt can be observed in hand sample (Figure 19). The rock slab is a 13 cm cross-section from a sill that was in direct contact with limestone at Merry Widow. As observed, the sill contains diagnostic skarn and boundary melt layers, analogous to the layers seen in many other dykes sampled at site. Furthermore, sulfide mineralization can be mapped along the dyke profile and used as a proxy for sulfide saturation. Interestingly, sulfides minerals observed in the basaltic hand sample are very coarse-grained and can be seen with the naked eye. As illustrated, the sulfide minerals are present within the dyke interior with the largest concentration between 5-8 cm from the limestone contact. Outside this range, the sulfide minerals appear less coarse and their concentration decreases. Within the boundary melt region, there is no appearance of any sulfides in hand sample. Instead, these sulfides are microcrystalline and contain a very low modal percentage. Finally, the skarn layer at the limestone contact is vibrant with sulfide minerals. Henceforth, sill 58B provides a real-life example for the distribution of sulfide minerals within these mafic dykes and can be contrasted to the empirical distribution using SCSS.

Comparison of the sill sample with the SCSS plot highlights that the two contain an identical distribution of sulfides. This equivalence illustrates that sulfide saturation is highly dependent on the process of limestone assimilation for these dykes. Melt along the limestone contact is silica-undersaturated and CaO rich from limestone assimilation. The assimilation process enhances the melt's capacity to transport sulfur and leads to sulfur-undersaturation within the boundary melt layer.

Consequently, sulfur species do not precipitate within the boundary melt as observed in Figure 19. Whereas inefficient mixing within dykes allows the interior melt to remain silica-saturated and promotes sulfide precipitation. Based on calculations and observations within the sill sample, the critical point of sulfur saturation is ~2.5 cm from the limestone contact. Regions past this limit will contain melts above the saturation limit and readily precipitate sulfide minerals. The caveat being that the melt must contain sufficient dissolved sulfur species and interact with limestone wallrock.

The implications of SCSS are critical for the formation of ore deposits. Mineral deposits such as IOCG (iron oxide copper gold), Fe-skarn, and even Cu-Ni PGE (platinum group element) deposits heavily rely on sulfide melt immiscibility in to concentrate chalcophile elements within a melt chamber (Chen, 2013; Nielsen et al., 2015, D'Souza & Canil, 2018). An efficient way to change sulfur saturation is by assimilating carbonate rock. Even a low degree of sulfide supersaturation will result in sulfide globules forming that efficiently scavenge metals, resulting in high concentrations (~38 mol%) of CuS and NiS in the earliest sulfide liquids (Zelenski et al., 2018). In addition to primary sulfide minerals, the sulfide globules can also concentrate other metals and attain sufficient ore grades for Au, Ag, Co, Bi, Se, Te, In and/or U, LREE, F, Ba, Mo (Skirrow, 2022). Sulfide immiscibility has been the proposed trigger for select world-class skarn deposits including Pine Creek tungsten (California), Twin Buttes copper (Arizona), and Bingham Canyon copper (Utah), USA, OK Tedi gold-copper (Papua New Guinea), and Avebury nickel (Tasmania) (Haldar, 2018).

9.4. Future Work

Extensive research has been undertaken to study the geochemical exchange that go on during the assimilation of limestone into basaltic melt. As outlined in this thesis, the partial mixing process generates super-enrichment Sr values within the dykes that are much higher than the endmember compositions. In addition, the most elevated Sr concentrations are reported within the interior of the dyke despite being sourced from the limestone at the contact Future experimentation could be carried out to explore and simulate the imputable causes that had led to the observed over-enrichment of Sr within these dykes. A few hypotheses have been proposed such as uphill diffusion of Sr or open system cycling of Sr through dyke melt-back (Morris et al., 2023; Bruce and Huppert, 1989). However, these processes have not been rigorously studied and lag modern-day analogues.

In addition, sulfur saturation has also been quantified along a single dyke profile. This profile helps formulate the changes in SCSS within a melt that has interacted with limestone. To help solidify this process further, a larger dataset must be analyzed and cross-referenced using hand samples. Further studies could also be conducted within the mineralized skarn layer which contains a large abundance of sulfide minerals. It could be hypothesized that the sulfides within the boundary melt layer migrate towards the limestone contact and are subsequently deposited to produce the skarn.

10. Conclusion

Using both bulk dyke and milli-slices from a single dyke profile, I have completed a geochemical survey of the Merry Widow Mountain dykes. Dyke samples that have undergone limestone assimilation report unique trace element enrichment patterns for Rb, Sr, U, Na_2O and MnO. The Sr abundance ranged greatly from 995 ppm to 2,645 ppm with its maximum much higher than its endmember compositions. One process to explain the super-enriched Sr values is by using a mixing model with a theoretical limestone value. Model estimates require up to 80 wt% mixing of the theoretical limestone with Bonanza Arc rocks to explain the dyke enrichment in Sr. Furthermore, the model highlights that the assimilation process could generate up to 35 wt% CO_2 during the decarbonization of limestone into basaltic dykes as it transcends the crust.

In addition, sulfide saturation was empirically calculated throughout a single dyke profile. The SCSS calculations emphasize that dykes carry a higher capacity to transport sulfur species adjacent to the dyke. This capacity declines threefold when moving ~24 cm into the dyke interior. The trend in SCSS is imputable to limestone assimilation where the mixing of limestone causes both desilication and calcium contamination that increases the saturation limit along the contact (Iacono Marziano et al., 2008; Carter and Dasgupta, 2016). The net result produced by assimilation of carbonate rock is the generation of an immiscible sulfide melt that can efficiently scavenge chalcophile elements for later deposition in an ore body (Haldar, 2018). Furthermore, the SCSS data corroborates with hand sample and thin section studies collected from site.

11. References

Barnes, C.G., Prestvik, T., Sundvoll, B., Surratt, D., 2005. Pervasive assimilation of carbonate and silicate rocks in the Hortavær igneous complex, north-central Norway. Lithos, Granitic Systems 80, 179–199. https://doi.org/10.1016/j.lithos.2003.11.002.

Bruce, P.M., Huppert, H.E., 1989. Thermal control of basaltic fissure eruptions. Nature 342, 665–667. https://doi.org/10.1038/342665a0.

Canil, D., Morris, R.A., 2023. Continentalization of an intraoceanic arc as exemplified by the Jurassic Bonanza arc of Vancouver Island, Canada. GSA Bulletin 136, 880–892. https://doi.org/10.1130/B36716.1.

Canil, D., Styan, J., Larocque, J., Bonnet, E., Kyba, J., 2010. Thickness and composition of the Bonanza arc crustal section, Vancouver Island, Canada. GSA Bulletin 122, 1094–1105. https://doi.org/10.1130/B26578.1.

Carter, L.B., Dasgupta, R., 2016. Effect of melt composition on crustal carbonate assimilation: Implications for the transition from calcite consumption to skarnification and associated CO2 degassing. Geochemistry, geophysics, geosystems: G3 17, 3893–3916.

Chadwick, J.P., Troll, V.R., Ginibre, C., Morgan, D., Gertisser, R., Waight, T.E., Davidson, J.P., 2007. Carbonate Assimilation at Merapi Volcano, Java, Indonesia: Insights from Crystal Isotope Stratigraphy. Journal of Petrology 48, 1793–1812. https://doi.org/10.1093/petrology/egm038.

Chen, H., 2013. External sulphur in IOCG mineralization: Implications on definition and classification of the IOCG clan. Ore Geology Reviews 51, 74–78. https://doi.org/10.1016/j.oregeorev.2012.12.002.

D'Souza, R.J., Canil, D., 2018. Effect of alkalinity on sulfur concentration at sulfide saturation in hydrous basaltic andesite to shoshonite melts at 1270 °C and 1 GPa. American Mineralogist 103, 1030–1043. https://doi.org/10.2138/am-2018-6404.

Dygert, N., Draper, D.S., Rapp, J.F., Lapen, T.J., Fagan, A.L., Neal, C.R., 2020. Experimental determinations of trace element partitioning between plagioclase, pigeonite, olivine, and lunar basaltic melts and an *f*O2 dependent model for plagioclase-melt Eu partitioning. Geochimica et Cosmochimica Acta 279, 258–280. https://doi.org/10.1016/j.gca.2020.03.037.

Faure, G., 1997. Principles and Applications of Geochemistry, 2nd Edition.

Greene, A.R., Scoates, J.S., Weis, D., Nixon, G.T., Kieffer, B., 2009. Melting History and Magmatic Evolution of Basalts and Picrites from the Accreted Wrangellia Oceanic Plateau, Vancouver Island, Canada. Journal of Petrology 50, 467–505. https://doi.org/10.1093/petrology/egp008.

Haldar, S.K., 2018. Chapter 2 - Economic Mineral Deposits and Host Rocks, in: Haldar, S.K. (Ed.), Mineral Exploration (Second Edition). Elsevier, pp. 25–45. https://doi.org/10.1016/B978-0-12-814022-2.00002-2.

Higgins, J.A., Blättler, C.L., Lundstrom, E.A., Santiago-Ramos, D.P., Akhtar, A.A., Crüger Ahm, A.-S., Bialik, O., Holmden, C., Bradbury, H., Murray, S.T., Swart, P.K., 2018. Mineralogy, early marine diagenesis, and the

chemistry of shallow-water carbonate sediments. Geochimica et Cosmochimica Acta 220, 512–534. https://doi.org/10.1016/j.gca.2017.09.046.

Iacono Marziano, G., Gaillard, F., Pichavant, M., 2008. Limestone assimilation by basaltic magmas: an experimental re-assessment and application to Italian volcanoes. Contributions to Mineralogy and Petrology 155, 719–738. https://doi.org/10.1007/s00410-007-0267-8.

Jochum, K.P., Nohl, U., Herwig, K., Lammel, E., Stoll, B., Hofmann, A.W., 2005. GeoReM: A New Geochemical Database for Reference Materials and Isotopic Standards. Geostandards and Geoanalytical Research 29, 333–338. https://doi.org/10.1111/j.1751-908X.2005.tb00904.x.

Jones, D.L., Silberling, N.J., Hillhouse, J., 1977. Wrangellia—A displaced terrane in northwestern North America. Canadian journal of earth sciences 14, 2565–2577.

Kahle, C.F., 1965. Strontium in oolitic limestones. Journal of Sedimentary Research 35, 846–856. https://doi.org/10.1306/74D7137F-2B21-11D7-8648000102C1865D.

Kelemen, P.B., Manning, C.E., 2015. Reevaluating carbon fluxes in subduction zones, what goes down, mostly comes up. Proceedings of the National Academy of Sciences 112, E3997–E4006. https://doi.org/10.1073/pnas.1507889112.

Lee, C.-T.A., Shen, B., Slotnick, B.S., Liao, K., Dickens, G.R., Yokoyama, Y., Lenardic, A., Dasgupta, R., Jellinek, M., Lackey, J.S., Schneider, T., Tice, M.M., 2013. Continental arc–island arc fluctuations, growth of crustal carbonates, and long-term climate change. Geosphere 9, 21–36. https://doi.org/10.1130/GES00822.1.

Lund, J.C., 1966. Structural geology of Empire mine, Empire Development Company Limited, Port McNeill, B.C. University of British Columbia. https://doi.org/10.14288/1.0053040.

Mason, E., Edmonds, M., Turchyn, A.V., 2017. Remobilization of crustal carbon may dominate volcanic arc emissions. Science (American Association for the Advancement of Science) 357, 290–294.

McLinden, C.A., Fioletov, V., Shephard, M.W., Krotkov, N., Li, C., Martin, R.V., Moran, M.D., Joiner, J., 2016. Space-based detection of missing sulfur dioxide sources of global air pollution. Nature Geoscience 9, 496–500. https://doi.org/10.1038/ngeo2724.

Morris, R., Canil, D., 2019. Raw trace element geochemistry for Quatsino limestone sampled at Merry Widow Mountain area. Internal source.

Morris, R., Canil, D., 2019. Skarn mineralization along magma-carbonate contacts in the Merry Widow Mountain area, Vancouver Island, British Columbia (NTS 092L). Geoscience BC Summary of Activities 2020–01.

Morris, R., Canil, D., 2020. Skarn Mineralization along Magma-Carbonate Contacts in the Merry Widow Mountain Area, Vancouver Island, British Columbia (NTS 092L). https://doi.org/10.13140/RG.2.2.19195.13601.

Morris, R., Canil, D., 2022. CO_2 transport at shallow depths in arc magmas: evidence from unique orbicular dikes in the Jurassic Bonanza arc, Vancouver Island, Canada. Contributions to mineralogy and petrology 177.

Morris, R.A., Canil, D., Spence, J., 2023. Magma-carbonate interactions drive CO_2 production and metal enrichment in shallow dikes and sills at volcanic arcs. Geology 52, 135–140. https://doi.org/10.1130/G51439.1.

Natale, J., Vitale, S., Giordano, G., Fedele, L., Lucci, F., Vona, A., Prinzi, E.P., Tramparulo, F.D., Isaia, R., Ciarcia, S., 2023. The Taverna San Felice Dike (NE of Roccamonfina Volcano): Unraveling Magmatic Intrusion Processes and Volcano-Tectonics in the Tyrrhenian Margin of the Southern Apennines. Geochemistry, Geophysics, Geosystems 24, e2023GC010994. https://doi.org/10.1029/2023GC010994.

Nielsen, T.F.D., Andersen, J.C.Ø., Holness, M.B., Keiding, J.K., Rudashevsky, N.S., Rudashevsky, V.N., Salmonsen, L.P., Tegner, C., Veksler, I.V., 2015. The Skaergaard PGE and Gold Deposit: The Result of in situ Fractionation, Sulphide Saturation, and Magma Chamber-scale Precious Metal Redistribution by Immiscible Fe-rich Melt. Journal of Petrology 56, 1643–1676. https://doi.org/10.1093/petrology/egv049

O'Neill, H.St.C., 2021. The Thermodynamic Controls on Sulfide Saturation in Silicate Melts with Application to Ocean Floor Basalts, in: Magma Redox Geochemistry. American Geophysical Union (AGU), pp. 177–213. https://doi.org/10.1002/9781119473206.ch10.

Paton, C., Hellstrom, J., Paul, B., Woodhead, J. Hergt, J., 2011. Iolite: Freeware for the visualisation and processing of mass spectrometric data. Journal of Analytical Atomic Spectrometry. doi:10.1039/c1ja10172b.

Paulson, B.D., 2010, Magmatic Processes in the Jurassic Bonanza Arc: Insights from the Alberni Region of Vancouver Island, Canada [M.Sc. thesis]: Bellingham, Washington, Western Washington University, 121.

Ray, G.E., Webster, I.C.L., 1991. Geology and mineral occurrences of the Merry Widow skarn camp, northern Vancouver Island. BC Ministry of Energy, Mines and Petroleum Resources, BC Geological Survey, Open File 1991-08, scale 1, 5000.

Skirrow, R.G., 2022. Iron oxide copper-gold (IOCG) deposits – A review (part 1): Settings, mineralogy, ore geochemistry and classification. Ore Geology Reviews 140, 104569. https://doi.org/10.1016/j.oregeorev.2021.104569.

Tanaka, K., MIURA, N., Asahara, Y., Kawabe, I., 2003. Rare earth element and strontium isotopic study of seamount-type limestones in Mesozoic accretionary complex of Southern Chichibu Terrane, central Japan: Implication for incorporation process of seawater REE into limestones. GEOCHEMICAL JOURNAL 37. https://doi.org/10.2343/geochemj.37.163

Weill, D.F., Drake, M.J., 1973. Europium Anomaly in Plagioclase Feldspar: Experimental Results and Semiquantitative Model. Science 180, 1059–1060.

Wong, K., Mason, E., Brune, S., East, M., Edmonds, M., Zahirovic, S., 2019. Deep Carbon Cycling Over the Past 200 Million Years: A Review of Fluxes in Different Tectonic Settings. Frontiers in earth science (Lausanne) 7.

Xu, Xinyue, Xu, Xiaochun, Szmihelsky, M., Yan, J., Xie, Q., Steele-MacInnis, M., 2023. Melt inclusion evidence for limestone assimilation, calc-silicate melts, and "magmatic skarn." Geology 51, 491–495. https://doi.org/10.1130/G50893.1.

Zelenski, M., Kamenetsky, V.S., Mavrogenes, J.A., Gurenko, A.A., Danyushevsky, L.V., 2018. Silicate-sulfide liquid immiscibility in modern arc basalt (Tolbachik volcano, Kamchatka): Part I. Occurrence and compositions of sulfide melts. Chemical Geology 478, 102–111. https://doi.org/10.1016/j.chemgeo.2017.09.013.

12. Appendices

12.1. Bulk Dyke Raw Data

Table 1: Mean major and trace element abundances for dyke margins (B) and interiors (A). Bulk dyke samples were analyzed as glass beads using LA-ICP-MS. Major elements reported in weight percentage and trace element in ppm.

Sample	*67A*	*67B*	*68A*	*68B*	*70B*	*89A*	*89B*	*165A*	*165B*	*168A*	*168B*
Na_2O	3.19	2.97	3.67	3.93	5.79	12.35	6.44	2.63	1.20	7.76	6.08
MgO	7.00	6.25	6.72	5.94	3.48	2.57	2.54	5.49	6.87	3.00	2.81
Al_2O_3	21.4	20.2	16.6	16.7	18.5	22.0	16.5	18.1	15.8	14.6	13.5
SiO_2	55.6	50.1	53.7	54.8	60.5	87.9	67.3	50.2	53.1	63.8	59.9
P_2O_5	0.17	0.17	0.23	0.25	0.75	0.73	0.80	0.17	0.33	0.75	0.73
K_2O	0.37	0.29	0.44	0.26	1.02	0.12	3.10	0.48	1.16	0.29	0.68
^{42}CaO	12.89	12.89	9.53	9.50	8.39	7.45	7.45	14.20	19.39	8.28	7.23
^{43}CaO	12.91	13.02	9.75	9.62	8.53	7.58	7.54	14.24	19.92	8.45	7.13
Sc	34	35	34	31	23	26	27	30	38	23	22
TiO_2	1.11	1.02	1.40	1.40	2.11	1.54	1.82	1.19	1.82	1.67	1.51
V	255	225	289	278	131	52	86	254	312	56	60
Cr_2O_3	0.01	0.01	0.00	0.00	0.00	0.00	0.00	0.01	0.00	0.00	0.00
MnO_2	0.18	0.15	0.17	0.14	0.16	0.12	0.14	0.15	0.26	0.15	0.20
FeO*	8.66	6.86	9.94	9.71	8.31	5.68	7.81	6.02	6.69	5.73	11.82
Co	39	18	28	34	6	19	26	21	21	3	6
Ni	47	30	30	28	5	4	1	36	21	1	2
^{63}Cu	75	18	74	86	14	57	135	9	7	12	18
^{65}Cu	73	17	73	88	13	52	136	9	8	9	17
Zn	50	43	54	51	48	44	52	55	48	26	53
Rb	7.7	4.7	11.4	6.1	20.6	2.6	51.6	9.1	32.1	4.2	3.1
Sr	498	471	627	516	2836	460	933	602	1077	1417	1414
Y	20	20	23	24	52	78	63	19	24	55	54
Zr	55	60	67	69	206	359	283	50	92	254	233
Nb	2	2	3	3	9	13	10	2	4	10	9
Ba	96	85	82	85	220	17	664	72	345	40	63
La	4.5	5.0	6.1	5.9	11.8	32.1	17.8	3.6	8.0	12.6	15.6
Ce	11.79	11.80	16.19	16.40	33.41	92.46	50.24	10.24	21.75	37.80	45.29
Pr	1.82	1.77	2.33	2.39	4.75	11.78	7.26	1.57	3.02	5.59	6.36
Nd	8.8	8.2	10.8	11.5	23.6	53.3	34.6	7.9	14.4	27.5	30.4
Sm	2.7	2.4	3.2	3.2	7.1	13.1	9.2	2.5	4.0	8.0	8.3
Eu	1.14	0.93	1.15	1.06	2.62	3.09	2.67	0.78	1.64	2.22	2.39
Gd	3.18	2.95	3.65	3.74	8.52	13.28	9.99	2.95	4.13	9.12	9.28
Tb	0.55	0.51	0.64	0.63	1.43	2.16	1.66	0.50	0.65	1.49	1.48
Dy	3.65	3.43	4.07	4.06	9.66	13.59	10.61	3.29	4.25	9.83	9.71
Ho	0.75	0.74	0.87	0.88	1.93	2.84	2.28	0.72	0.88	2.02	2.03
Er	2.17	2.15	2.49	2.52	5.57	8.02	6.43	2.00	2.56	5.79	5.85
Tm	0.33	0.33	0.39	0.37	0.75	1.20	0.99	0.30	0.38	0.84	0.84
Yb	2.17	2.12	2.49	2.49	5.12	7.77	6.53	2.03	2.59	5.79	5.75
Lu	0.33	0.32	0.36	0.37	0.78	1.12	0.97	0.30	0.38	0.86	0.87
Hf	1.57	1.75	1.91	1.89	4.99	8.26	6.66	1.47	2.68	6.01	5.55
Ta	0.13	0.14	0.15	0.15	0.52	0.76	0.56	0.12	0.23	0.56	0.52
Pb	1.43	0.61	0.97	0.79	0.60	1.09	1.82	0.75	0.76	0.66	1.82
Th	0.68	0.79	0.80	0.84	1.57	3.12	2.37	0.52	1.19	2.22	2.11
U	0.36	0.35	0.52	0.50	0.92	1.66	1.33	0.27	1.10	1.08	1.45
Sr/Sr*	3.15	3.50	3.53	2.79	7.59	0.52	1.67	4.83	4.63	3.24	2.88
Eu/Eu*	1.18	1.07	1.03	0.93	1.03	0.71	0.85	0.88	1.23	0.79	0.83

FeO * is the total iron in both oxidation states.

Table 2: Major and trace element limit of detections (LOD) for dyke margins (B) and interiors (A). Bulk dyke samples were analyzed as glass beads using LA-ICP-MS. Major elements reported in weight percentage and trace element in ppm.

Sample	*67A*	*67B*	*68A*	*68B*	*70B*	*89A*	*89B*	*165A*	*165B*	*168A*	*168B*
Na_2O	0.0002	0.0001	0.0002	0.0001	0.0001	0.0002	0.0001	0.0001	0.0001	0.0001	0.0002
MgO	0.00005	0.00004	0.00004	0.00004	0.00003	0.00003	0.00004	0.00004	0.00004	0.00003	0.00004
Al_2O_3	0.00004	0.00003	0.00003	0.00003	0.00003	0.00003	0.00002	0.00003	0.00003	0.00002	0.00003
SiO_2	0.004	0.003	0.004	0.003	0.003	0.004	0.003	0.004	0.003	0.003	0.004
P_2O_5	0.0008	0.0007	0.0008	0.0007	0.0007	0.0010	0.0008	0.0007	0.0007	0.0008	0.0008
K_2O	0.00004	0.00004	0.00004	0.00004	0.00004	0.00005	0.00004	0.00004	0.00004	0.00004	0.00004
^{42}CaO	0.001	0.001	0.001	0.001	0.001	0.002	0.001	0.001	0.001	0.001	0.001
^{43}CaO	0.003	0.002	0.003	0.002	0.002	0.003	0.002	0.003	0.002	0.002	0.003
Sc	0.03	0.02	0.02	0.02	0.02	0.03	0.02	0.02	0.02	0.02	0.02
TiO_2	0.00003	0.00002	0.00002	0.00003	0.00002	0.00002	0.00002	0.00002	0.00002	0.00002	0.00002
V	0.01	0.01	0.01	0.01	0.01	0.01	0.01	0.01	0.01	0.01	0.01
Cr_2O_3	0.00002	0.00002	0.00002	0.00002	0.00002	0.00003	0.00002	0.00002	0.00002	0.00002	0.00002
MnO_2	0.00001	0.00000	0.00001	0.00001	0.00001	0.00001	0.00001	0.00001	0.00001	0.00001	0.00001
FeO*	0.0004	0.0004	0.0004	0.0004	0.0004	0.0005	0.0004	0.0004	0.0004	0.0004	0.0004
Co	0.02	0.01	0.02	0.01	0.02	0.02	0.01	0.01	0.01	0.02	0.02
Ni	0.08	0.06	0.08	0.07	0.08	0.08	0.08	0.08	0.07	0.07	0.08
^{63}Cu	0.03	0.03	0.04	0.03	0.03	0.04	0.03	0.03	0.03	0.04	0.04
^{65}Cu	0.03	0.03	0.03	0.03	0.03	0.04	0.03	0.03	0.03	0.03	0.04
Zn	0.05	0.05	0.05	0.05	0.05	0.06	0.04	0.05	0.05	0.04	0.05
Rb	0.002	0.002	0.002	0.001	0.002	0.002	0.002	0.001	0.002	0.002	0.001
Sr	0.005	0.008	0.002	0.003	0.005	0.003	0.004	0.003	0.004	0.003	0.006
Y	0.001	0.001	0.001	0.001	0.001	0.001	0.002	0.001	0.001	0.001	0.001
Zr	0.002	0.002	0.003	0.002	0.004	0.004	0.004	0.002	0.002	0.003	0.005
Nb	0.0005	0.0007	0.0004	0.0006	0.0014	0.0011	0.0006	0.0005	0.0006	0.0003	0.0008
Ba	0.007	0.007	0.003	0.005	0.005	0.003	0.007	0.003	0.014	0.003	0.003
La	0.0002	0.0006	0.0002	0.0006	0.0005	0.0011	0.0005	0.0002	0.0009	0.0008	0.0007
Ce	0.0004	0.0007	0.0005	0.0007	0.0005	0.0012	0.0012	0.0003	0.0010	0.0011	0.0010
Pr	0.0002	0.0002	0.0002	0.0004	0.0002	0.0005	0.0004	0.0003	0.0002	0.0004	0.0004
Nd	0.0025	0.0010	0.0027	0.0015	0.0023	0.0043	0.0032	0.0018	0.0032	0.0024	0.0020
Sm	0.0013	0.0020	0.0013	0.0013	0.0021	0.0016	0.0013	0.0013	0.0014	0.0013	0.0029
Eu	0.0007	0.0007	0.0004	0.0008	0.0007	0.0005	0.0004	0.0004	0.0007	0.0004	0.0004
Gd	0.0032	0.0012	0.0026	0.0032	0.0024	0.0035	0.0038	0.0031	0.0025	0.0013	0.0021
Tb	0.0002	0.0004	0.0002	0.0003	0.0002	0.0005	0.0003	0.0002	0.0002	0.0003	0.0005
Dy	0.0009	0.0008	0.0009	0.0009	0.0009	0.0016	0.0009	0.0009	0.0017	0.0009	0.0008
Ho	0.0002	0.0002	0.0002	0.0002	0.0002	0.0004	0.0004	0.0002	0.0002	0.0004	0.0002
Er	0.0007	0.0006	0.0011	0.0007	0.0007	0.0008	0.0007	0.0012	0.0011	0.0007	0.0011
Tm	0.0002	0.0004	0.0004	0.0004	0.0004	0.0004	0.0004	0.0004	0.0002	0.0002	0.0004
Yb	0.0010	0.0009	0.0010	0.0010	0.0010	0.0022	0.0011	0.0010	0.0019	0.0018	0.0010
Lu	0.0002	0.0003	0.0002	0.0002	0.0002	0.0004	0.0002	0.0004	0.0002	0.0004	0.0002
Hf	0.0008	0.0007	0.0008	0.0013	0.0017	0.0010	0.0008	0.0008	0.0008	0.0008	0.0015
Ta	0.0003	0.0002	0.0002	0.0002	0.0003	0.0003	0.0003	0.0003	0.0003	0.0003	0.0002
Pb	0.0023	0.0028	0.0023	0.0022	0.0026	0.0030	0.0021	0.0022	0.0029	0.0025	0.0028
Th	0.0003	0.0003	0.0003	0.0003	0.0005	0.0006	0.0007	0.0003	0.0003	0.0003	0.0003
U	0.0003	0.0004	0.0002	0.0002	0.0003	0.0006	0.0004	0.0002	0.0003	0.0002	0.0005

FeO * is the total iron in both oxidation states.

12.2. Raw Milli-Slice Raw Data

Table 3: Mean major and trace element abundances for milli-slices sampled from dyke 79B profile. Milli-slices were analyzed as glass beads using LA-ICP-MS. Major elements reported in weight percentage and trace element in ppm.

Milli-slice interval	*#1*	*#2*	*#3*	*#4*	*#5*	*#10*	*#20*	*#30*	*#40*	*#50*	*#60*	*#70*	*#80*	*#90*
Distance from LST contact (cm)	**0.5**	**0.75**	**1**	**1.25**	**1.5**	**2.5**	**5.3**	**8**	**10.7**	**13.7**	**16.3**	**18.9**	**21.5**	**24.1**
Na_2O	0.35	0.53	2.39	3.06	3.64	4.30	3.60	4.20	4.87	4.48	5.13	5.21	6.58	9.26
MgO	3.64	3.41	3.52	3.55	3.41	4.00	4.28	5.90	7.73	6.13	6.48	5.95	5.42	4.06
Al_2O_3	10.1	14.0	13.0	11.9	12.9	14.2	14.3	17.9	24.5	21.4	21.6	21.7	19.6	25.0
SiO_2	38.7	40.8	41.0	42.5	44.4	50.2	48.1	55.3	65.1	60.2	65.5	64.7	70.3	83.2
P_2O_5	0.45	0.37	0.35	0.30	0.32	0.37	0.78	0.35	0.26	0.35	0.35	0.32	0.82	0.97
K_2O	0.33	0.72	0.57	0.37	0.42	0.51	0.63	0.77	0.99	0.90	1.03	1.03	1.15	1.17
^{42}CaO	20.99	19.24	14.20	12.87	12.54	12.00	12.00	12.00	12.00	12.00	12.00	12.00	12.00	12.00
^{43}CaO	21.02	19.46	14.19	13.06	12.65	12.13	12.09	12.07	12.30	11.94	12.06	11.90	12.19	11.95
Sc	33	40	38	29	37	43	25	48	42	50	49	44	36	35
TiO_2	1.74	2.06	2.07	1.49	1.80	2.13	1.49	2.37	2.12	2.69	2.65	2.69	1.87	2.16
V	299	273	315	260	279	330	202	425	390	449	466	423	244	113
Cr_2O_3	0.00	0.00	0.00	0.00	0.00	0.00	0.00	0.00	0.00	0.00	0.00	0.00	0.00	0.00
MnO_2	0.46	0.35	0.37	0.34	0.31	0.28	0.27	0.26	0.23	0.26	0.26	0.27	0.26	0.20
FeO*	12.58	13.75	13.77	13.62	12.63	10.67	21.50	13.78	15.43	15.43	15.41	15.64	17.19	8.23
Co	18	13	17	17	16	18	116	37	27	40	42	32	84	17
Ni	4	3	7	7	5	4	23	16	18	18	22	13	21	2
^{63}Cu	61	15	51	42	21	17	606	68	29	69	84	42	198	19
^{65}Cu	60	15	50	42	20	17	599	67	28	69	86	42	197	19
Zn	97	102	129	101	94	80	94	120	115	117	125	123	89	85
Rb	6.2	15.1	4.9	2.9	3.6	3.1	3.8	10.0	16.0	15.1	18.2	14.9	8.0	11.2
Sr	1384	2645	1364	1041	995	1273	1729	1771	1820	1851	2042	2037	2315	2459
Y	32	35	38	43	50	45	66	42	25	43	42	44	76	79
Zr	134	164	137	197	194	168	260	143	91	146	143	141	314	343
Nb	5	5	5	5	5	5	8	4	3	5	5	5	9	12
Ba	292	545	160	96	111	121	98	116	182	125	202	147	178	447
La	5.2	6.9	7.5	16.7	13.4	10.4	20.1	8.6	6.8	8.8	9.5	10.2	17.6	17.1
Ce	15.82	21.04	19.30	39.49	32.17	25.73	48.72	21.82	18.02	22.90	24.25	26.21	41.17	44.19
Pr	2.61	3.27	2.98	5.74	4.74	3.86	7.09	3.33	2.57	3.49	3.64	4.01	6.05	6.70
Nd	13.2	15.3	15.1	27.3	23.2	19.1	34.4	16.8	12.5	18.1	18.1	20.4	30.7	33.7
Sm	3.8	4.2	4.7	6.8	6.6	5.5	9.5	5.0	3.4	5.5	5.3	5.8	9.0	10.0
Eu	1.05	0.60	0.76	2.22	2.03	1.66	2.75	1.90	1.77	1.96	2.01	2.56	3.52	2.64
Gd	4.58	5.43	5.82	7.92	7.91	7.03	11.22	6.35	4.05	6.76	6.51	6.94	11.09	11.88
Tb	0.80	0.94	1.01	1.20	1.29	1.15	1.78	1.08	0.66	1.13	1.10	1.16	1.90	2.00
Dy	5.23	6.10	6.55	7.64	8.62	7.55	11.43	6.98	4.20	7.44	7.18	7.56	12.55	13.36
Ho	1.12	1.30	1.37	1.59	1.75	1.60	2.34	1.48	0.89	1.53	1.51	1.57	2.65	2.83
Er	3.49	3.97	4.14	4.69	5.55	4.96	7.26	4.54	2.74	4.75	4.75	4.73	8.39	8.55
Tm	0.51	0.57	0.58	0.67	0.78	0.71	1.02	0.65	0.40	0.67	0.67	0.66	1.21	1.24
Yb	3.39	3.65	3.77	4.70	5.14	4.74	6.81	4.34	2.72	4.46	4.40	4.66	8.00	7.75
Lu	0.53	0.56	0.57	0.72	0.83	0.73	1.08	0.66	0.41	0.70	0.67	0.68	1.26	1.26
Hf	3.39	4.18	3.51	4.94	4.98	4.13	6.52	3.73	2.38	3.86	3.65	3.69	7.65	8.26
Ta	0.27	0.32	0.30	0.34	0.37	0.35	0.52	0.29	0.19	0.30	0.29	0.28	0.61	0.81
Pb	0.36	0.62	0.37	0.47	0.72	0.61	0.78	0.69	0.77	0.72	0.74	0.66	0.55	2.63
Th	0.99	1.23	1.01	1.58	1.45	1.26	2.12	0.97	0.55	0.95	0.98	0.91	2.28	2.56
U	7.71	3.36	0.96	0.96	0.81	0.58	0.81	0.45	0.32	0.45	0.47	0.53	0.84	0.99
Sr/Sr*	6.66	10.58	5.75	2.35	2.69	4.20	3.13	6.71	9.08	6.61	7.12	6.39	4.81	4.63
Eu/Eu*	0.76	0.38	0.44	0.92	0.86	0.81	0.81	1.03	1.45	0.98	1.05	1.23	1.08	0.74

FeO * is the total iron in both oxidation states.

Table 4: Major and trace element LOD for milli-slices sampled from dyke 79B profile. Milli-slices were analyzed as glass beads using LA-ICP-MS. Major elements reported in weight percentage and trace element in ppm.

Milli-slice interval	*#1*	*#2*	*#3*	*#4*	*#5*	*#10*	*#20*	*#30*	*#40*	*#50*	*#60*	*#70*	*#80*	*#90*
Distance from LST contact (cm)	**0.5**	**0.75**	**1**	**1.25**	**1.5**	**2.5**	**5.3**	**8**	**10.7**	**13.7**	**16.3**	**18.9**	**21.5**	**24.1**
Na_2O	0.0018	0.0025	0.0019	0.0021	0.0019	0.0020	0.0021	0.0022	0.0037	0.0025	0.0026	0.0027	0.0027	0.0032
MgO	0.0007	0.0006	0.0006	0.0007	0.0006	0.0007	0.0008	0.0007	0.0013	0.0010	0.0010	0.0011	0.0012	0.0014
Al_2O_3	0.0005	0.0007	0.0005	0.0007	0.0006	0.0006	0.0006	0.0007	0.0011	0.0008	0.0009	0.0008	0.0009	0.0010
SiO_2	0.0507	0.0698	0.0539	0.0589	0.0545	0.0594	0.0628	0.0688	0.1146	0.0771	0.0820	0.0835	0.0854	0.1035
P_2O_5	0.0050	0.0070	0.0053	0.0058	0.0053	0.0056	0.0059	0.0064	0.0105	0.0070	0.0075	0.0078	0.0078	0.0095
K_2O	0.0001	0.0001	0.0001	0.0001	0.0001	0.0001	0.0001	0.0001	0.0001	0.0001	0.0001	0.0001	0.0001	0.0001
^{42}CaO	0.0027	0.0038	0.0029	0.0031	0.0028	0.0030	0.0032	0.0034	0.0056	0.0038	0.0039	0.0040	0.0041	0.0047
^{43}CaO	0.0074	0.0102	0.0078	0.0084	0.0078	0.0085	0.0087	0.0092	0.0155	0.0101	0.0105	0.0106	0.0106	0.0126
Sc	0.0526	0.0766	0.0571	0.0618	0.0554	0.0602	0.0639	0.0680	0.1103	0.0746	0.0790	0.0787	0.0791	0.0916
TiO_2	0.0000	0.0000	0.0000	0.0000	0.0000	0.0000	0.0000	0.0000	0.0001	0.0001	0.0000	0.0001	0.0001	0.0001
V	0.0335	0.0451	0.0355	0.0359	0.0331	0.0350	0.0345	0.0391	0.0651	0.0433	0.0455	0.0453	0.0442	0.0500
Cr_2O_3	0.0000	0.0000	0.0000	0.0000	0.0000	0.0000	0.0000	0.0000	0.0000	0.0000	0.0000	0.0000	0.0000	0.0000
MnO_2	0.0000	0.0000	0.0000	0.0000	0.0000	0.0000	0.0000	0.0000	0.0000	0.0000	0.0000	0.0000	0.0000	0.0000
FeO*	0.0004	0.0005	0.0004	0.0004	0.0004	0.0004	0.0004	0.0004	0.0007	0.0005	0.0005	0.0005	0.0005	0.0009
Co	0.0187	0.0298	0.0215	0.0238	0.0197	0.0229	0.0230	0.0265	0.0452	0.0304	0.0298	0.0302	0.0283	0.0355
Ni	0.0746	0.1013	0.0759	0.0852	0.0755	0.0721	0.0729	0.0883	0.1520	0.0965	0.1038	0.1106	0.1067	0.1186
^{63}Cu	0.1026	0.1409	0.1054	0.1125	0.1083	0.1139	0.1229	0.1291	0.2123	0.1392	0.1483	0.1536	0.1502	0.1780
^{65}Cu	0.1513	0.2139	0.1642	0.1758	0.1578	0.1650	0.1824	0.1905	0.3182	0.2006	0.2112	0.2318	0.2291	0.2589
Zn	0.0832	0.1056	0.0895	0.1030	0.0990	0.0877	0.1077	0.1078	0.1689	0.1151	0.1141	0.1295	0.1221	0.1389
Rb	0.0024	0.0034	0.0036	0.0032	0.0027	0.0026	0.0038	0.0033	0.0058	0.0054	0.0053	0.0042	0.0026	0.0057
Y	0.0017	0.0022	0.0008	0.0011	0.0019	0.0015	0.0020	0.0021	0.0024	0.0026	0.0019	0.0021	0.0021	0.0024
Zr	0.0033	0.0036	0.0019	0.0037	0.0019	0.0039	0.0062	0.0030	0.0029	0.0040	0.0045	0.0094	0.0090	0.0094
Nb	0.0002	0.0020	0.0008	0.0002	0.0010	0.0002	0.0014	0.0009	0.0021	0.0018	0.0019	0.0012	0.0066	0.0014
Ba	0.0321	0.0015	0.0143	0.0114	0.0093	0.0017	0.0067	0.0124	0.0027	0.0122	0.0143	0.0090	0.0028	0.0241
La	0.0009	0.0002	0.0002	0.0002	0.0011	0.0002	0.0010	0.0011	0.0018	0.0014	0.0002	0.0018	0.0014	0.0028
Ce	0.0011	0.0002	0.0010	0.0010	0.0019	0.0017	0.0021	0.0025	0.0023	0.0015	0.0021	0.0020	0.0029	0.0004
Pr	0.0008	0.0002	0.0007	0.0002	0.0002	0.0002	0.0009	0.0002	0.0020	0.0008	0.0002	0.0016	0.0013	0.0004
Nd	0.0037	0.0009	0.0009	0.0010	0.0075	0.0011	0.0067	0.0059	0.0017	0.0012	0.0012	0.0071	0.0060	0.0105
Sm	0.0010	0.0011	0.0011	0.0012	0.0046	0.0013	0.0012	0.0013	0.0021	0.0060	0.0015	0.0034	0.0022	0.0026
Eu	0.0003	0.0035	0.0003	0.0015	0.0003	0.0004	0.0004	0.0025	0.0006	0.0004	0.0004	0.0021	0.0006	0.0008
Gd	0.0010	0.0011	0.0011	0.0011	0.0011	0.0013	0.0012	0.0012	0.0020	0.0014	0.0014	0.0083	0.0021	0.0025
Tb	0.0009	0.0002	0.0002	0.0002	0.0002	0.0002	0.0002	0.0002	0.0003	0.0002	0.0002	0.0017	0.0003	0.0004
Dy	0.0007	0.0007	0.0007	0.0051	0.0008	0.0044	0.0008	0.0008	0.0014	0.0009	0.0041	0.0046	0.0014	0.0017
Ho	0.0002	0.0012	0.0002	0.0002	0.0008	0.0002	0.0002	0.0002	0.0003	0.0002	0.0010	0.0006	0.0004	0.0014
Er	0.0005	0.0006	0.0006	0.0025	0.0006	0.0007	0.0006	0.0006	0.0011	0.0007	0.0007	0.0058	0.0037	0.0042
Tm	0.0007	0.0002	0.0002	0.0002	0.0002	0.0002	0.0002	0.0002	0.0003	0.0002	0.0002	0.0006	0.0004	0.0004
Yb	0.0008	0.0009	0.0009	0.0009	0.0009	0.0010	0.0053	0.0010	0.0016	0.0011	0.0012	0.0027	0.0017	0.0020
Lu	0.0002	0.0002	0.0002	0.0002	0.0002	0.0002	0.0002	0.0002	0.0004	0.0003	0.0003	0.0006	0.0004	0.0005
Hf	0.0006	0.0007	0.0007	0.0007	0.0007	0.0008	0.0041	0.0008	0.0013	0.0009	0.0009	0.0021	0.0013	0.0015
Ta	0.0002	0.0002	0.0002	0.0002	0.0009	0.0002	0.0002	0.0002	0.0004	0.0003	0.0003	0.0006	0.0004	0.0005
Pb	0.0046	0.0036	0.0041	0.0060	0.0046	0.0065	0.0072	0.0080	0.0102	0.0088	0.0033	0.0102	0.0064	0.0080
Th	0.0003	0.0020	0.0003	0.0003	0.0003	0.0018	0.0003	0.0003	0.0006	0.0004	0.0004	0.0009	0.0020	0.0007
U	0.0003	0.0003	0.0003	0.0003	0.0003	0.0003	0.0003	0.0003	0.0005	0.0004	0.0004	0.0009	0.0006	0.0007

FeO * is the total iron in both oxidation states.

12.3. External Standard Raw Data

Table 5: Mean major and trace element abundances for the external standard KL2-G and duplicate milli-slice #60. KL2-G trial runs 1 and 2 were gathered during the data collection process for the bulk dyke samples (Dec 2023), while trials 3-5 were taken during milli-slice collection period (Jan 2024) using LA-ICP-MS. Major elements reported in weight percentage and trace element in ppm.

Sample	KL2-G Trial 1	KL2-G Trial 2	KL2-G Trial 3	KL2-G Trial 4	KL2-G Trial 5	#60 Dup
Na_2O	2.46	2.25	2.41	2.38	2.41	5.38
MgO	7.32	6.91	7.39	7.39	6.86	5.86
Al_2O_3	13.4	12.8	13.2	13.3	12.8	18.2
SiO_2	49.5	46.5	49.6	50.6	48.0	56.6
P_2O_5	0.27	0.25	0.28	0.27	0.26	0.38
K_2O	0.49	0.46	0.49	0.48	0.48	1.0
^{42}CaO	10.90	10.90	0.00	0.00	0.00	12.00
^{43}CaO	11.02	10.89	11.09	10.65	10.83	12.01
Sc	32	32	33	32	32	52
TiO_2	2.62	2.49	2.62	2.54	2.58	2.88
V	317	288	322	311	306	480
Cr_2O_3	0.04	0.04	0.04	0.04	0.04	0.00
MnO_2	0.17	0.16	0.17	0.16	0.17	0.28
FeO*	11.00	10.00	11.12	10.84	10.52	16.22
Co	43	40	44	42	42	47
Ni	111	104	107	105	109	26
^{63}Cu	96	86	92	88	91	91
^{65}Cu	94	90	92	88	94	91
Zn	86	81	97	92	90	144
Rb	9.1	8.2	9	9	8	17
Sr	372	352	370	357	355	2030
Y	26	26	28	27	27	45
Zr	156	151	164	156	160	154
Nb	16	15	15	15	15	5
Ba	123	109	125	122	121	195
La	13.5	13.2	13.7	13.1	13.2	10.1
Ce	34.34	32.94	33.73	32.68	33.25	25.98
Pr	4.82	4.63	4.81	4.58	4.65	3.90
Nd	22.1	22.3	23.0	21.4	22.2	18.9
Sm	5.6	5.8	5.9	5.6	5.8	5.6
Eu	2.02	1.96	2.01	1.91	1.92	2.06
Gd	5.95	5.94	6.34	6.18	6.02	6.76
Tb	0.91	0.90	0.97	0.90	0.91	1.16
Dy	5.43	5.33	5.53	5.45	5.50	7.44
Ho	0.99	0.96	1.07	0.98	1.00	1.54
Er	2.61	2.55	2.78	2.73	2.73	4.67
Tm	0.36	0.34	0.37	0.35	0.37	0.69
Yb	2.15	2.07	2.18	2.16	2.13	4.54
Lu	0.29	0.29	0.30	0.30	0.30	0.69
Hf	3.99	3.94	4.34	4.12	4.09	3.67
Ta	0.95	0.93	1.00	0.95	0.95	0.29
Pb	1.87	1.67	1.70	1.87	1.87	0.72
Th	1.02	0.96	1.07	1.03	1.07	0.98
U	0.53	0.50	0.53	0.50	0.53	0.47

FeO * is the total iron in both oxidation states.

Table 6: Major and trace element LOD for the external standard KL2-G and duplicate milli-slice #60. KL2-G trial runs 1 and 2 were gathered during the data collection process for the bulk dyke samples (Dec 2023), while trials 3-5 were taken during milli-slice collection period (Jan 2024) using LA-ICP-MS. Major elements reported in weight percentage and trace element in ppm.

Sample	KL2-G Trial 1	KL2-G Trial 2	KL2-G Trial 3	KL2-G Trial 4	KL2-G Trial 5	#60 Dup
Na_2O	0.0001	0.0001	0.002	0.002	0.002	0.003
MgO	0.00004	0.00006	0.001	0.001	0.001	0.001
Al_2O_3	0.00002	0.00003	0.001	0.001	0.001	0.001
SiO_2	0.003	0.003	0.065	0.061	0.067	0.094
P_2O_5	0.0008	0.0006	0.006	0.006	0.006	0.009
K_2O	0.00004	0.00003	0.0001	0.0001	0.0001	0.0001
^{42}CaO	0.001	0.001	0.004	0.003	0.002	0.003
^{43}CaO	0.002	0.002	0.009	0.008	0.008	0.012
Sc	0.02	0.02	0.07	0.06	0.06	0.08
TiO_2	0.00002	0.00002	0.00005	0.00004	0.00004	0.00005
V	0.007	0.009	0.04	0.03	0.04	0.04
Cr_2O_3	0.00002	0.00002	0.00003	0.00002	0.00002	0.00002
MnO_2	0.000005	0.000004	0.00001	0.00001	0.00001	0.00002
FeO*	0.0004	0.0004	0.0005	0.0004	0.0004	0.0006
Co	0.01	0.01	0.03	0.02	0.02	0.03
Ni	0.08	0.06	0.11	0.08	0.08	0.12
^{63}Cu	0.03	0.03	0.13	0.11	0.11	0.17
^{65}Cu	0.03	0.03	0.20	0.17	0.18	0.25
Zn	0.05	0.03	0.11	0.10	0.09	0.10
Rb	0.001	0.002	0.00	0.00	0.00	0.01
Sr	0.002	0.005	0.00	0.00	0.01	0.01
Y	0.0009	0.0012	0.002	0.002	0.002	0.003
Zr	0.001	0.003	0.003	0.003	0.004	0.006
Nb	0.001	0.001	0.0012	0.0002	0.0014	0.0003
Ba	0.005	0.007	0.01	0.01	0.01	0.02
La	0.0007	0.0011	0.0002	0.0007	0.0007	0.0010
Ce	0.0002	0.0011	0.0009	0.0012	0.0002	0.0003
Pr	0.0004	0.0001	0.0008	0.0002	0.0009	0.0002
Nd	0.004	0.003	0.001	0.001	0.001	0.001
Sm	0.001	0.004	0.001	0.001	0.005	0.002
Eu	0.0004	0.0009	0.0021	0.0003	0.0020	0.0037
Gd	0.0012	0.0031	0.001	0.005	0.001	0.002
Tb	0.0002	0.0002	0.0008	0.0002	0.0002	0.0002
Dy	0.0008	0.0007	0.001	0.012	0.001	0.001
Ho	0.0002	0.0002	0.001	0.000	0.000	0.000
Er	0.0006	0.0005	0.003	0.001	0.001	0.001
Tm	0.0002	0.0002	0.0002	0.0002	0.0002	0.0003
Yb	0.0009	0.0008	0.001	0.001	0.001	0.001
Lu	0.0002	0.0005	0.0002	0.0002	0.0002	0.0003
Hf	0.0007	0.0023	0.004	0.001	0.003	0.001
Ta	0.0002	0.0002	0.0002	0.0002	0.0002	0.0003
Pb	0.003	0.003	0.006	0.003	0.007	0.011
Th	0.0003	0.0002	0.0004	0.0003	0.0003	0.0004
U	0.0002	0.0002	0.0003	0.0003	0.0003	0.0004

FeO * is the total iron in both oxidation states.

12.4. Quatsino Limestone Raw Data

Table 7: Four Triassic-age Quatsino limestone samples gathered from Merry Widow Mountain region (Morris and Canil, 2019). Trace element abundances collected using LA-ICP-MS.

limestone	69D	78D	165D	MW-QL
Sr (ppm)	602	720	622	252
Sr/Sr*	242.39	493.62	144.22	66.51
Eu/Eu*	0.90	1.01	0.82	0.81